First-In-Class Thiosemicarbazone Metal Complexes Targeting the Sigma-2 Receptor (S2R) as an Innovative Strategy against Pancreatic Cancer

Alessandra Barbanente,[#] Joanna Kopecka,[#] Daniele Vitone, Mauro Niso, Rosanna Rizzi, Corrado Cuocci, Francesca Serena Abatematteo, Francesco Mastropasqua, Nicola Antonio Colabufo, Nicola Margiotta, Fabio Arnesano, Chiara Riganti,* and Carmen Abate*

Read Online

ACCESS | Metrics & More | Article Recommendations | Supporting Information

ABSTRACT: Pancreatic cancer, with its increasing incidence and lowest 5-year survival rate, is predicted to become the second leading cause of cancer deaths by 2030. Current clinical trials have shown limited improvement, highlighting the need for new therapies. The sigma-2 receptor (S2R), with roles in tumor progression, is a target for novel thiosemicarbazones (TSCs). **FA4** has shown potent activity against pancreatic cancer *in vivo*. We synthesized complexes of **FA4** with Cu(II) and Pt(II), and compared their efficacy with complexes of the non-S2R-targeting TSC **1**. TSC-Cu exhibited over 50-fold higher *in vitro* cytotoxicity than TSCs-Pt, which was less active than TSCs. **FA4**-Cu induced apoptotic cell death *via* ER and mitochondrial stress showing more potent activity than **FA4**. This *in vitro* effect was replicated in the preclinical PANC-1 model, where **FA4**-Cu was more potent than **FA4**, **1**, and **1**-Cu. These results support further exploration of **FA4**-Cu as a potential therapy for pancreatic cancer.
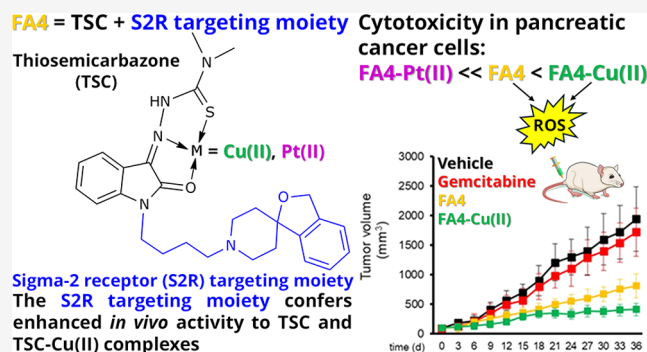
INTRODUCTION

S2R has been investigated for decades as a target related to psychosis or tumor progression. Overexpressed in a wide variety of tumors with its ligands exerting anticancer activity, S2R has received interest as a promising target for tumor treatment and diagnosis.[1−4] Overexpressed also in the central nervous system (CNS), the S2R has more lately been investigated as a target for the treatment of Alzheimer's disease (AD) as it appears to be particularly expressed in the neurons of AD patients in proximity to the Aβ oligomers in synapses[5] where it would interfere with Aβ 1−42 oligomers binding to neurons and the subsequent neurotoxic cascade.[6,7] Several clinical studies were carried out with the compound named Elayta, now in the clinical phase for the treatment of mild to moderate AD.

Despite this scientific interest, the identity of the S2R has remained elusive for decades and only recently the receptor has been cloned and structurally characterized as the transmembrane protein of the endoplasmic reticulum (ER) TMEM97.[8] This identity, together with the S2R ligands developed over the years, has fueled scientific enthusiasm in the definition of the mechanism of action of this still enigmatic receptor. While 20-(S)-hydroxycholesterol has been proposed as a TMEM97 endogenous ligand,[9] a protein−protein interaction map is beginning to take shape. A ternary complex of S2R with progesterone receptor component 1 (PGRMC1) and low-density lipoprotein (LDL) receptor has been shown to modulate the internalization of LDL.[10] In pancreatic and breast cancer cells, the association of S2R with the translocator protein (TSPO), a mitochondrial transmembrane protein with cholesterol binding/transporter properties, was demonstrated, further supporting the involvement of S2R in cholesterol metabolism and transport.[11] More recently, the interaction of S2R with the epigenetic reader BAHCC1[12] in retinal cells has been demonstrated, shedding light on the possible mechanism connecting TMEM97 to retinal degeneration. This discovery underscores the protective effect of S2R ligands against dry age-related macular degeneration (dry-AMD).[13,14]

A highly promising class of novel thiosemicarbazones (TSCs) targeting S2R has been recently developed.[15−17] Given the increasing evidence suggesting the effectiveness of
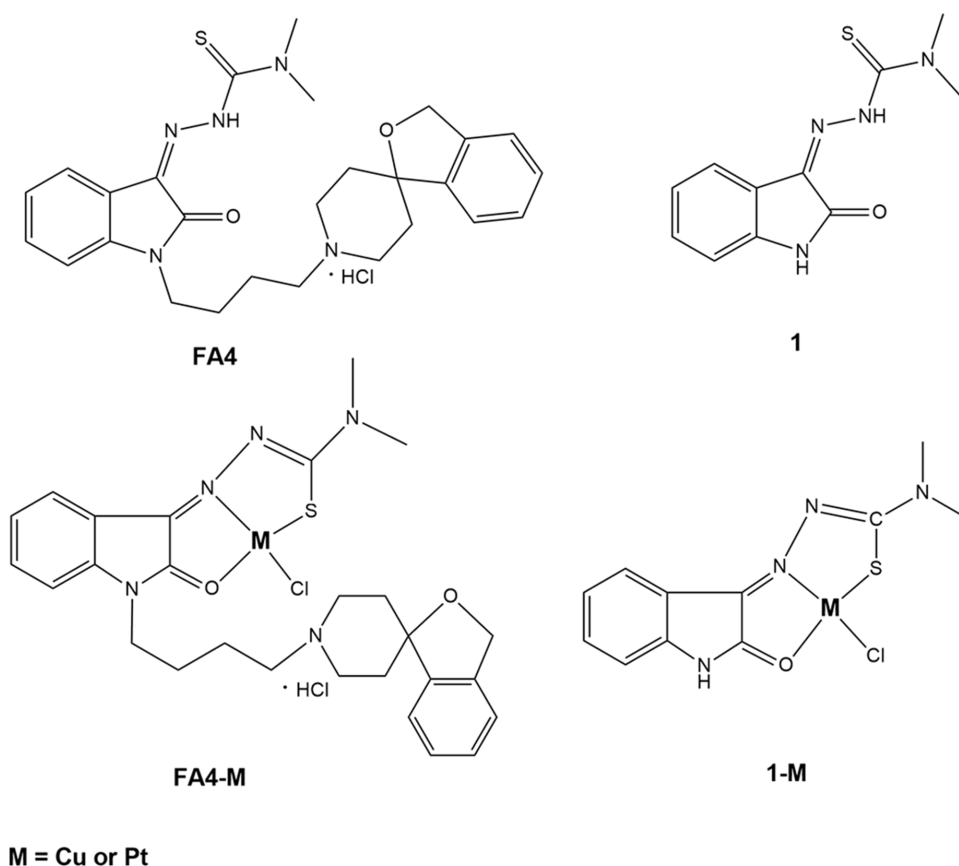
M = Cu or Pt

Figure 1. S2R-targeting thiosemicarbazone (**FA4**·HCl) and thiosemicarbazone devoid of the S2R-targeting portion (**1**) and their respective metal complexes (M = Cu(II) or Pt(II)).

compounds modulating metal metabolism against aggressive cancers, we developed TSCs targeting S2R, leveraging their ability to bind metal ions, such as iron and copper. Research in this field has evolved along two main paths. On one hand, redox metal ions like iron and copper can induce metalloplasia, a newly recognized form of regulated metal-dependent cell growth and proliferation that can be therapeutically targeted with metal-selective chelators.[18] On the other hand, they trigger ferro/cuproptosis, a type of cell death characterized by cytotoxicity stemming from increased mitochondria-dependent energy metabolism and the accumulation of reactive oxygen species (ROS), which can be activated by metallophores.[19,20]

While all TSCs, differing for the S2R-targeting basic moiety, exhibited cytotoxic potential and showed promising results in preclinical *in vivo* studies, the most favorable outcomes across all tested cells were observed with (*Z*)-2-(1-(4-(3*H*-spiro-[isobenzofuran-1,4′-piperidine]-1′-yl)butyl)-2-oxoindolin-3-ylidene)-*N*,*N*-dimethylhydrazinecarbothioamide hydrochloride (**FA4**, Figure 1).[15,16,18,21] Notably, an analogue of **FA4** lacking the metal-chelating moiety, i.e., 1′-(4-(1*H*-indol-1-yl)butyl)-3*H*-spiro[isobenzofuran-1,4′-piperidine], exhibited reduced cytotoxicity in pancreatic cells.[22] Conversely, (*Z*)-*N*,*N*-dimethyl-2-(2-oxoindolin-3-ylidene)hydrazinecarbothioamide (**1**, Figure 1), lacking the S2R-targeting moiety, demonstrated *in vivo* toxicity (nephropathy and pulmonary toxicity) in a pancreatic tumor model.[15] These findings supporting the positive synergistic effect of combining the metal-chelating portion with the S2R-targeting moiety were further validated by a recent study. In this work, the activity of S2R ligands capable of coordinating metals was associated with their ability

to coordinate copper ions in models of pancreatic cancer.[23] The promising data obtained with **FA4** in an aggressive pancreatic tumor, whose incidence rate continues to rise with poor prognosis, motivated us to explore the generation of copper complexes of TSCs. This approach leverages the reported improved activity of metal complexes compared to the corresponding free ligands.[24,25] Additionally, platinum complexes of TSCs were synthesized, given the capability of Pt(II) compounds to induce cytotoxicity in cancer cells. Indeed, despite its side effects, cisplatin (*cis*-diamminedichloridoplatinum(II)), remains one of the most successful anticancer compounds used in clinics for various cancers, including testicular, ovarian, and gastrointestinal malignancies.[26,27] Mononuclear and polynuclear platinum complexes displaying good cytotoxic activities have already been prepared with bidentate or tridentate-coordinated TSCs.[28,29] Notably, complexes featuring TSC ligands with the general formula [Pt(TSC)Cl] have shown reduced nephrotoxicity against normal cells compared to that with cisplatin. For example, the [Pt(TSC)Cl] complex containing the *N*-(4)-phenyl-2-formylpyridine thiosemicarbazone (HTSC) was found to be toxic against the colon cancer Caco-2 cell line in a cell cycle-dependent manner. It induced cell death *via* caspase-mediated apoptosis and exhibited reduced nephrotoxic potential compared to cisplatin.[30]

Tridentate Pt(II)-coordinated TSCs attracted our attention due to their potential resemblance to monofunctional Pt(II) complexes with the general formula *cis*-[Pt(NH$_3$)$_2$(*N*-heterocycle)Cl]Cl. Mononuclear Pt(II) complexes have gained attention for their ability to bind DNA at a single site, inducing
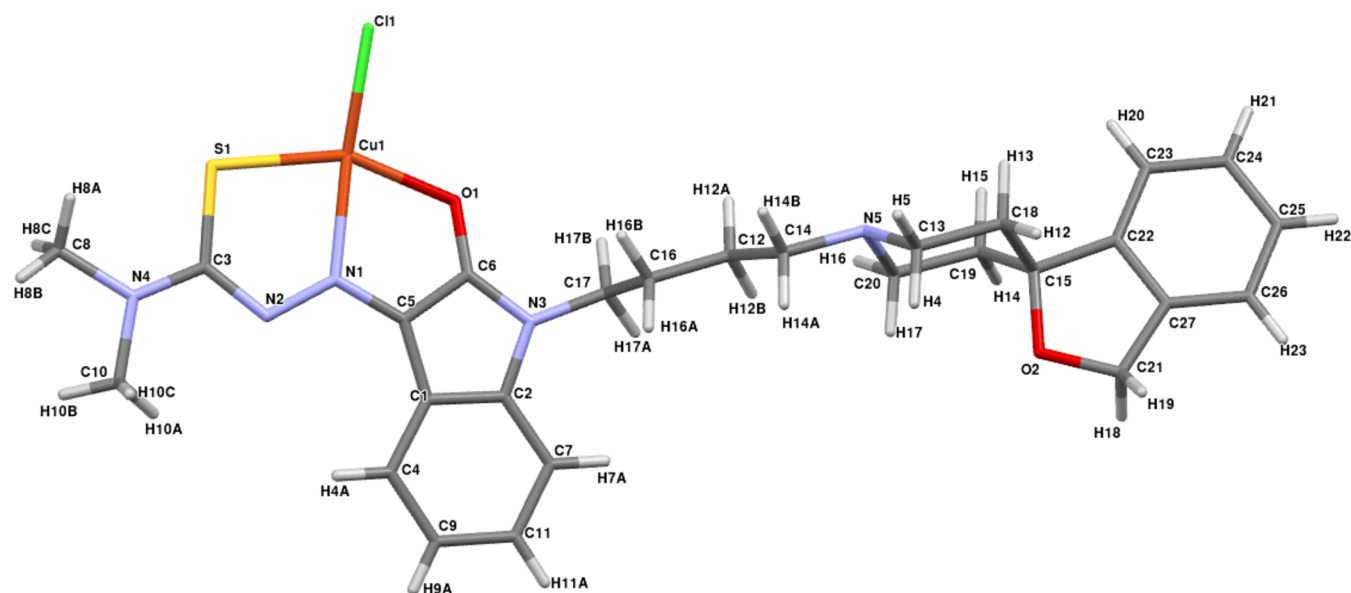
Figure 2. Asymmetric unit of **FA4**-Cu, showing the atomic numbering scheme. Color legend: carbon (light gray), hydrogen (white), oxygen (red), nitrogen (light blue), chlorine (green), and sulfur (yellow). Crystallographic data were deposited at the Cambridge Structural Database (CSD) with CCDC number 2351856.

minimal distortion in the double helix and demonstrating significant antitumor properties. This offers a distinct spectrum of activity compared to classical bifunctional cross-linking agents like cisplatin.[31−34] Among them, phenanthriplatin (*cis*-[Pt(NH$_3$)$_2$(phenanthridine)Cl]NO$_3$) has emerged as one of the most effective compounds, exhibiting significantly greater activity than cisplatin and oxaliplatin. Studies on its reactivity toward cellular components have revealed efficient binding to nucleobases, a characteristic typically required for an active platinum drug, while showing delayed reactivity toward sulfur-containing nucleophiles associated with tumor resistance mechanisms.[31−34]

The choice of TSCs as ligands to coordinate Pt(II) ions is further motivated by their lipophilicity, which enhances complex permeability across cell membranes. Additionally, Pt-thiosemicarbazone complexes exhibit greater stability compared to Pt-glutathione adducts, which may potentially form in the cytoplasm.[35] This is particularly relevant as Pt-glutathione adducts have been implicated in contributing to cell resistance to Pt(II) anticancer drugs.

In summary, leveraging the synergistic relationship between our TSCs and the S2R-mediated activity, we report the synthesis, structural analysis, and biological activity of Cu(II) and Pt(II) complexes of TSCs **1** and **FA4** (general formula in Figure 1), with the focus on pancreatic cancer. The synthesis of metal complexes follows a targeted delivery strategy aimed at ascertaining whether the superior efficacy and reduced toxicity observed with S2R-targeting TSCs extend to these complexes, recognizing the elevated level of expression of S2R in various cancers, notably in pancreatic cancer.

RESULTS AND DISCUSSION

Chemistry. *Synthesis and Characterization of TSCs 1 and FA4 and Their Cu(II) and Pt(II) Complexes.* The synthesis of TSCs **1** and **FA4** was performed according to the previously reported procedures.[15,17] [CuCl(ACthio-1)] (**1**-Cu) was prepared by dissolving equimolar amounts of CuCl$_2$ and **1** in EtOH. The elemental analysis was in accordance with the

presence of **1**, Cu, and Cl in a 1:1:1 ratio. This was also confirmed by the ESI-MS(−) spectrum (electrospray mass spectrum recorded in negative ion mode), which showed a peak at m/z = 343.2835 corresponding to singly charged species [C$_{11}$H$_{11}$ON$_4$SCuCl−H]$^-$ (Figure S1A). The Fourier-transform infrared spectroscopy (FTIR) spectrum of **1**-Cu (Figure S2B) showed two emerging bands assigned to ν(Cu−S) and ν(Cu−Cl), and the two bands of ν(C=O) and ν(C=N) at lower frequencies (1652 and 1530 cm^{-1}, respectively) with respect to **1** (Figure S2A), suggesting Cu(II) coordination by the O atom of C=O and the imine N atom (Figure S1B).[36−38] The electronic absorption spectra of **1** in dimethylsulfoxide (DMSO) with increasing amounts of CuCl$_2$ showed an increase of the band at 440 nm, corresponding to the Cu(II) complex, with a maximum of intensity at 1 equivalent of CuCl$_2$ (Figure S1C).

[PtCl(ACthio-1)] (**1**-Pt) was prepared by following a two-step reaction. The precursor complex [PtCl$_2$(DMSO)$_2$] was obtained by treating K$_2$[PtCl$_4$] with an excess of DMSO in water. The Pt(II) precursor complex, which was chosen for its better solubility in alcohols with respect to the platinum salt, was then treated with **1** in equimolar amounts in MeOH and then treated with **1** in equimolar amounts, affording the desired compound **1**-Pt, which was characterized by elemental analysis, ESI-MS, and multinuclear one-dimensional space (1D) and two-dimensional (2D) nuclear magnetic resonance (NMR) spectroscopy, exploiting the diamagnetic Pt(II) ion in place of paramagnetic Cu(II). As in the case of **1**-Cu, both the elemental analysis and the ESI-MS data are in agreement with the formation of a complex having Pt, **1**, and Cl in a 1:1:1 ratio. The ESI-MS(−) spectrum showed the presence of a peak at m/z = 476.9909, corresponding to [C$_{11}$H$_{11}$ON$_4$SPtCl−H]$^-$, with the experimental isotopic pattern of the peak in good agreement with the theoretical one (Figure S3A). **1**-Pt was thoroughly characterized by 1D (^{1}H and ^{13}C; Figures S3B and S4B) and 2D ([^{1}H,^{13}C] HMBC, Figure S4B) NMR spectroscopy in DMF-d_7 to avoid possible solvation processes and the data obtained were compared to those of free **1** in the same
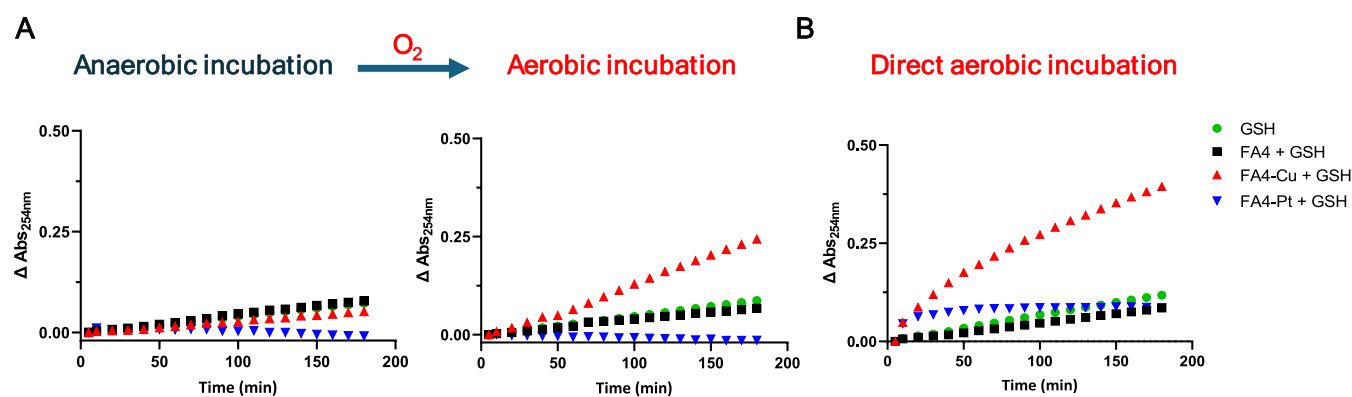
Figure 3. Reactivity of **FA4** and its Cu(II) and Pt(II) complexes with reduced glutathione (GSH). Time-dependent absorbance changes at 254 nm, monitored by UV−vis spectroscopy, for the indicated reaction mixtures incubated under anaerobic conditions followed by oxygen exposure (A) and under direct aerobic conditions (B). The increase in absorbance at 254 nm corresponds to the formation of oxidized glutathione (GSSG). Buffer: 100 mM HEPES pH 7.4; DMSO/DMF 5%; [**FA4**/**FA4**-Cu/**FA4**-Pt] = 30 μM; [GSH] = 3 mM.

solvent (Figure S4A). In particular, the 1D ^{13}C NMR spectra in DMF-d_7 of free **1** and **1**-Pt (Figure S3B) showed that C1, C9, and C12 are the most perturbed upon Pt(II) binding, resonating downfield with respect to the corresponding carbons in free **1** by 20.22, 6.52, and 11.24 ppm, respectively. This observation supports a Pt(II) coordination to **1** by the deprotonated thiolate, iminic N, and C=O oxygen atoms. As further evidence of the hypothesized coordination sphere, the ^{195}Pt NMR spectrum in DMF-d_7 (Figure S3C) shows a single peak at −2635.65 ppm, which is in the range typical for a Pt(II) atom in a SONCl coordination environment.[39]

[CuCl(FA4)] (**FA4**-Cu) was prepared by dissolving equimolar amounts of CuCl$_2$ and **FA4** in EtOH. The elemental analysis was in accordance with the presence of **FA4**, Cu, and Cl in a 1:1:1 ratio. Consistently, the ESI-MS(+) spectrum (recorded in positive ion mode) showed a peak at m/z 589.1329, which corresponds to the singly charged species $[C_{27}H_{32}O_2N_5SCuCl + H]^+$, indicating that the Cu(II) ion coordinates to one **FA4** molecule and a chloride ion (Figure S5A,B). The FTIR spectrum of **FA4**-Cu (Figure S6B) showed two emerging bands assigned to $\nu(\text{Cu−S})$ and $\nu(\text{Cu−Cl})$, and two bands of $\nu(\text{C=O})$ and $\nu(\text{C=N})$ at lower frequencies (1651 and 1598 cm^{-1}, respectively) with respect to **FA4** (Figure S6A), suggesting Cu(II) coordination by the O atom of C=O and the iminic N atom (Figure S5B). The electronic absorption spectra of **FA4** in DMSO with increasing amounts of CuCl$_2$ showed an increase of the absorption band at 431 nm, corresponding to the Cu(II) complex, with a maximum of intensity at 1 equivalent of CuCl$_2$ (Figure S5C).

The X-ray powder diffraction (XRPD) data, collected using a laboratory diffractometer, was employed for the structural characterization of **FA4**-Cu. Structure determination was automatically performed using the software EXPO,[40] which employs the simulated annealing algorithm for powder diffraction data. The resulting model was subsequently refined by using the Rietveld method. All the XRPD data for FA4-Cu are reported in Table S1. The asymmetric unit and the unit-cell content of the refined structure are shown in Figures 2 and S7, respectively.

[Pt(FA4)Cl] (**FA4**-Pt) was prepared similarly to **1**-Pt by treating the $[\text{PtCl}_2(\text{DMSO})_2]$ precursor complex with equimolar amounts of **FA4**, inducing precipitation of the desired compound with Et$_2$O. **FA4**-Pt was characterized by elemental analysis and ESI-MS, and also using 1D and 2D

NMR spectroscopy. The ESI-MS(+) spectrum (Figure S8A) showed the presence of a peak at m/z = 722.1674 corresponding to the singly charged species $[C_{27}H_{32}O_2N_5SPtCl + H]^+$, indicating that the Pt(II) ion coordinates to an **FA4** molecule and a chloride ion in a 1:1:1 ratio, as confirmed also by elemental analysis. **FA4**-Pt was characterized through 1D (^{1}H and ^{13}C; Figures S8B, S9B, and S10B) and 2D ($[^1$H,^{13}C] HSQC and $[^1$H,^{13}C] HMBC, Figures S9B and S10B, respectively) NMR spectroscopy in MeOD-d_4 and compared to those of free **FA4** in the same solvent (Figures S9A and S10A). The overlay of 1D ^{13}C NMR spectra of free **FA4** and **FA4**-Pt (Figure S8B) revealed the most significant downfield shifts for C1, C9, and C12 by 20.13, 4.15, and 12.17 ppm, respectively. This observation indicates that the Pt(II) ion is coordinated to **FA4** through the thiolate S, iminic N, and carbonyl O atoms. Consistently, the ^{195}Pt NMR spectrum in MeOD-d_4 (Figure S8C) showed a single peak at −2632.66 ppm, which is in the range typical for a Pt(II) atom in a SONCl coordination environment.[39]

Reactivity of FA4 and Its Cu(II) and Pt(II) Complexes with Glutathione and Transmetalation. Complexation of metal ions significantly influences the redox behavior of TSCs and their cytotoxicity. Recent results have demonstrated that TSC-Cu(II) complexes can catalyze the oxidation of GSH to GSSG faster than Cu(II) alone at neutral pH, thus accelerating ROS production.[41]

By ultraviolet−visible (UV−vis) spectroscopy, it is possible to monitor the oxidation of GSH to GSSG through the increase in absorbance at 254 nm.[25] As shown in Figures 3A and S11A, under anaerobic conditions, only a modest increase in absorbance is detected after 180 min of incubation of 3 mM GSH in HEPES buffer (pH 7.4). The same behavior is observed when the cuvette is exposed to oxygen for a further 180 min, indicating a slow oxidation of glutathione (GSH) even under aerobic conditions.

In the presence of 30 μM **FA4**, at a 1:100 molar ratio with GSH, the increase in absorbance at 254 nm is the same as for GSH alone, both in the absence and presence of oxygen, indicating no involvement of the free ligand in the oxidation process. In contrast, when **FA4**-Cu is present, there is a significant increase in absorbance at 254 nm under aerobic conditions, indicating a catalytic effect of the Cu(II) complex on GSH oxidation. Notably, with **FA4**-Pt, the absorbance at

Table 1. Cytotoxicity of TSCs 1 and FA4 and Their Metal Complexes in Pancreatic Cancer and Normal Cell Lines

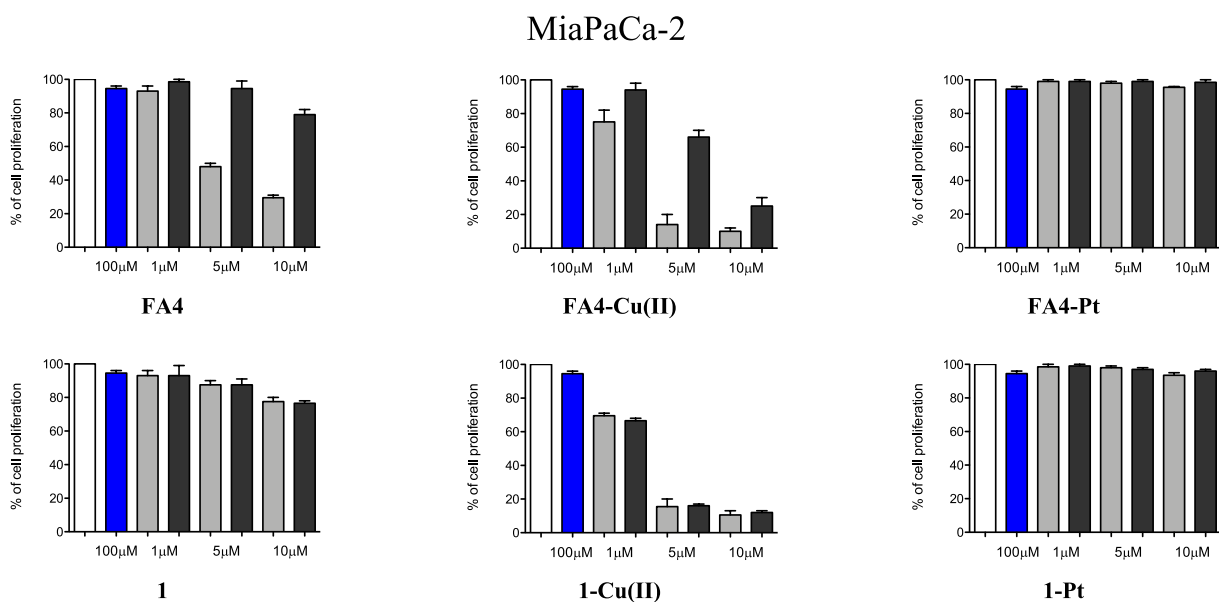|	antiproliferative effect (EC_{50} $\mu M \pm$ SEM)					
	PANC-1		MiaPaCa-2		HPDE	
compd	48 h	72 h	48 h	72 h	48 h	72 h
1	0.57 ± 0.10	0.55 ± 0.11	20.2 ± 2.1	18.1 ± 1.3	13.14 ± 1.3	8.15 ± 1.1
1-Cu	0.22 ± 0.06	0.26 ± 0.05	0.66 ± 0.13	0.63 ± 0.14	21.11 ± 2.3	9.02 ± 0.9
1-Pt	21.4 ± 1.5	19.8 ± 1.1	42.3 ± 3.1	38.9 ± 3.4	95.74 ± 7.6	36.48 ± 4.7
FA4	0.93 ± 0.21	0.71 ± 0.14	3.19 ± 0.71	1.74 ± 0.52	14.93 ± 1.8	2.2 ± 0.17
FA4-Cu	0.49 ± 0.09	0.48 ± 0.08	0.88 ± 0.15	0.85 ± 0.12	19.85 ± 2.3	3.91 ± 0.37
FA4-Pt	29.4 ± 2.1	16.0 ± 1.7	50.3 ± 3.1	29.4 ± 3.2	10.43 ± 2.1	39.13 ± 3.48

Figure 4. ROS involvement in the cytotoxicity exerted by TSCs **1** and **FA4** and their Cu(II) or Pt(II) complexes in MiaPaCa-2 (A) and PANC-1 (B) cells.
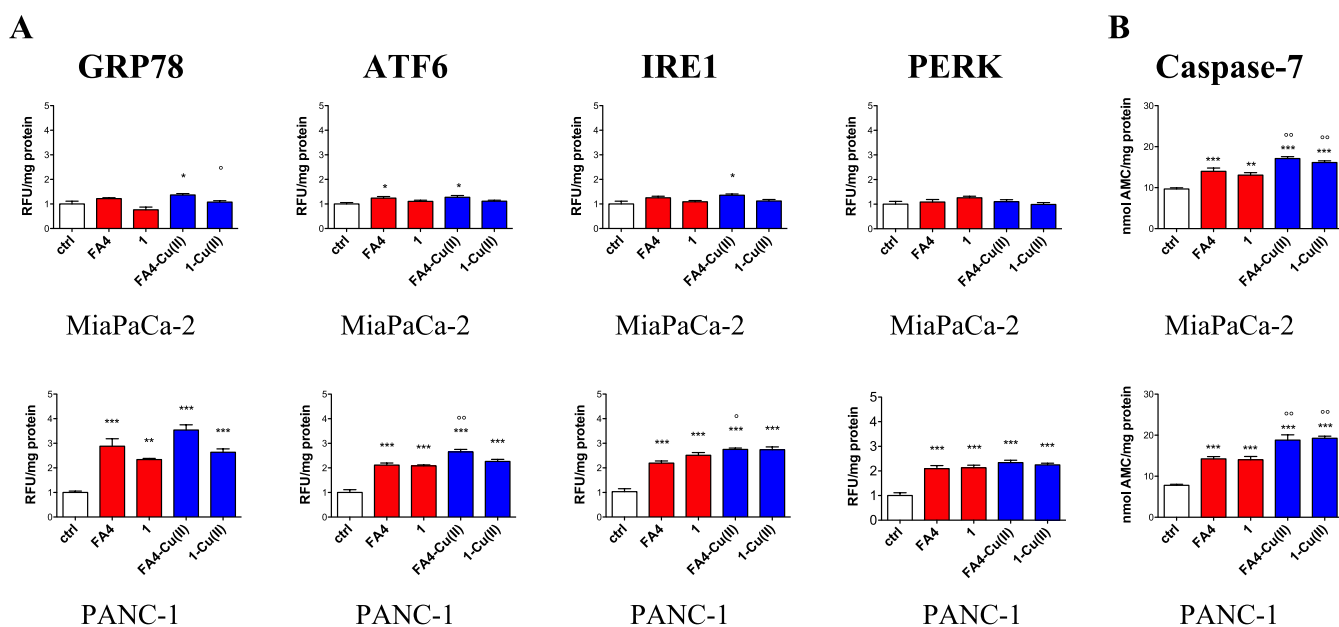
Figure 5. (A) Expression of ER stress gene sensors and (B) activation of caspase7 in MiaPaCa-2 and PANC-1 cells treated with **FA4**, **1**, and their Cu(II) complexes for 24 h at a 50 μM concentration. Data are means + SD (n = 3). *p < 0.05, **p < 0.01, ***p < 0.001 vs ctrl; °p < 0.05, °°p < 0.01, °°°P < 0.001: Cu(II)-coordinated vs respective uncoordinated compound.

254 nm remains very low throughout the entire incubation period (Figure 3A).

By monitoring the spectral changes at the absorption maxima of Cu(II) and Pt(II) complexes (422 nm in both cases) and the free ligand (354 nm) under anaerobic conditions (Figure S12A), very little or no change is observed for free **FA4**, as expected, while a slow decrease in absorbance of the Pt(II) complex and an increase in free **FA4** indicate slight dissociation of the Pt complex under excess GSH. In contrast, for the Cu(II) complex, the decrease in absorbance at 422 nm is not accompanied by a corresponding increase in the absorbance of the free ligand at 354 nm. Instead, a slight shift at longer wavelengths (~450 nm) is observed. Moreover, a significant decrease in absorbance at 422 nm occurs shortly after mixing **FA4**-Cu with GSH, indicating the rapid coordination of GSH to the Cu(II) complex and the formation of the ternary complex **FA4**-Cu-GSH, which serves as an intermediate in the catalytic mechanism of GSH oxidation. Upon exposure to oxygen, the spectral changes at 422 nm are less pronounced, likely due to reoxidation of the copper complex (Figure S12A).
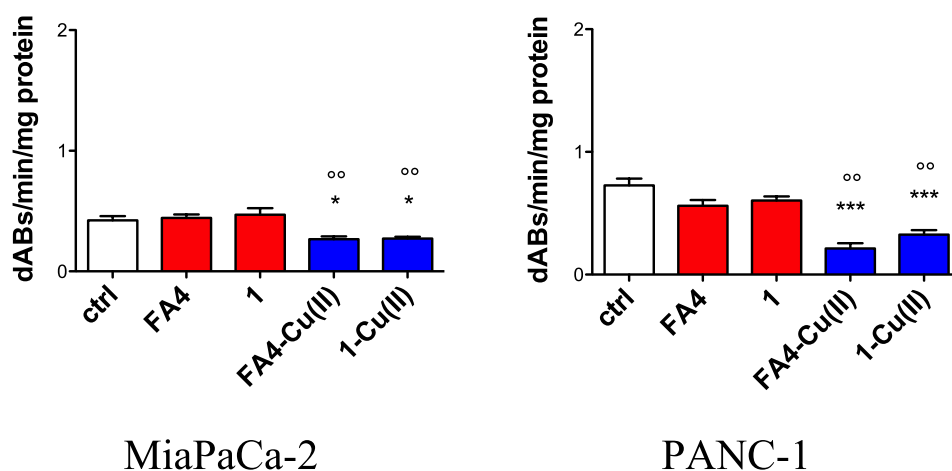
In a second set of experiments, the samples were aerated from the beginning (Figures S3B, S11B, and S12B). Similar spectral changes were observed across the various cases compared to the experiments with prior anaerobic incubation, with a notable difference being an earlier increase in absorbance at 254 nm in the case of **FA4**-Cu (Figure S3B). This is attributed to the immediate availability of oxygen as an electron acceptor, leading to faster GSSG formation. These results demonstrate that Cu(II) enhances, while Pt(II) inhibits, the redox activity of **FA4**.

A recent study demonstrated that Cu(II) transmetalation of Zn(II), Ga(III), and (to a lesser extent) Ni(II) complexes—unlike the inert Co(III) and Pd(II) complexes—positively affects the antiproliferative activity of Dp44 mT, another anticancer TSC.[42]
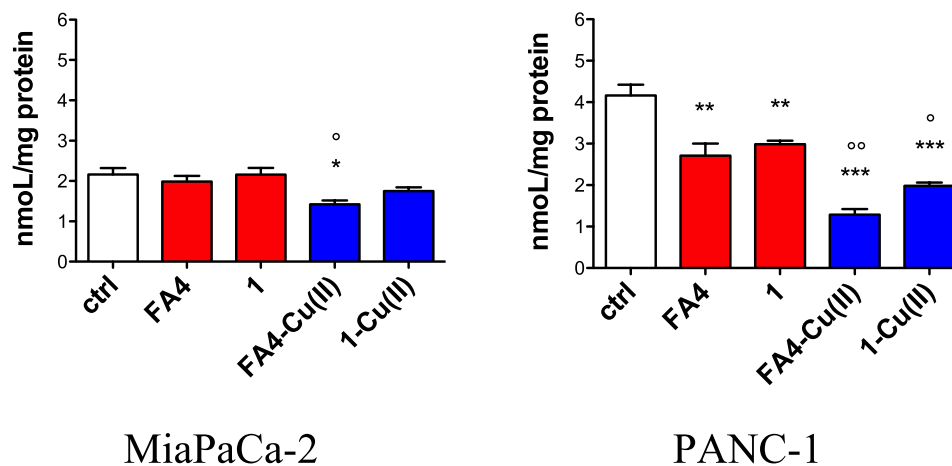
To investigate whether transmetalation of **FA4**-Pt can occur in the presence of a Cu(II) salt, we incubated **FA4**-Pt with 1 equivalent of $CuCl_2$ and recorded ESI-MS spectra after 24 h (Figure S13). The molecular peak of **FA4**-Pt (m/z = 722.1674) remained detectable at the end of the incubation, and no peak corresponding to the **FA4**-Cu complex (m/z = 589.1329) was observed. This indicates that **FA4**-Pt is resistant to transmetalation under these conditions, suggesting its inertness in cells and low cytotoxicity.

Biology. *Cytotoxic Activity in Pancreatic Cells.* The cytotoxicity of the Cu(II) and Pt(II) complexes was tested in the two pancreatic cell lines in which S2R-mediated activity was previously ascertained, and **FA4** had shown a promising antitumor activity engaging diverse death pathways, i.e., PANC-1 and MiaPaCa-2.[11,17] Herein, the complexes were challenged with the corresponding metal-free TSCs **1** and **FA4** (Table 1). In PANC-1 cells, a 2-fold increase in the antitumor activity was found for the Cu(II) complexes compared to the corresponding metal-free TSCs at 48 and 72 h, all displaying submicromolar EC_{50} values (from 0.22 to 0.85 μM). In MiaPaCa-2 cells, while **FA4** was slightly less potent than in PANC-1 (EC_{50} values 3.19 and 1.74 μM, at 48 and 72 h respectively), TSC **1** displayed a drastically reduced activity (EC_{50} values 20.2 and 18.1 μM, at 48 and 72 h, respectively). Despite this different activity of the two TSCs in MiaPaCa-2 cells, the corresponding Pt(II) complexes of compound **1** and **FA4** displayed a drastically reduced activity, also at the longer incubation time with EC_{50} values ranging from 19.8 μM to 50.3 μM (Table 1). Interestingly, in nontumoral human pancreatic epithelial HPDE cells, most compounds were less cytotoxic than in PDAC cells, except for the Pt(II) complexes whose activity was generally similar. The Cu(II) complexes did not exert a higher cytotoxicity than the parental compounds **1** and **FA4** (Table 1). These results suggest that TSC-Cu complexes exert preferential cytotoxicity on PDAC cells, exploiting specific features of cancer cells.
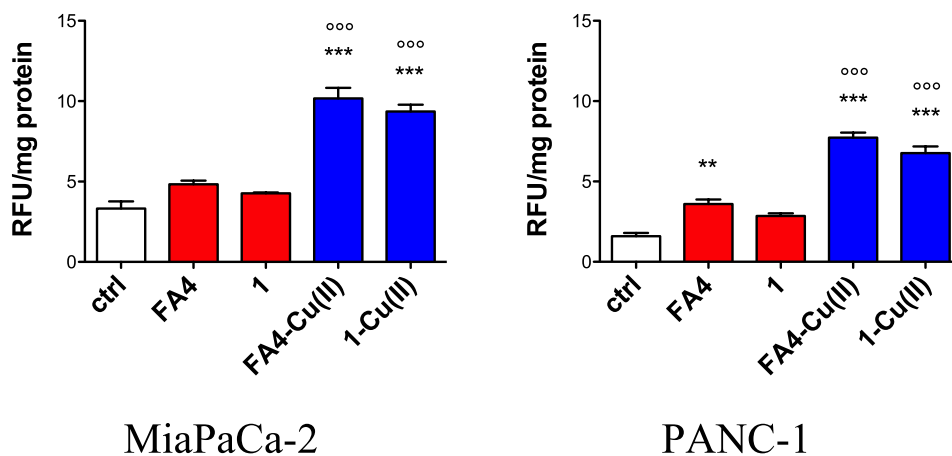
Figure 6. Electron transport chain (A), mitochondrial ATP (B), and ROS (C) in MiaPaCa-2 and PANC-1 cells treated with **FA4**, **1**, and their Cu(II) complexes for 24 h at 50 μM concentration. Data are means + SD ($n = 3$). $*p < 0.05$, $**p < 0.01$, $***p < 0.001$ vs ctrl; $°p < 0.05$, $°°p < 0.01$, $°°°p < 0.001$: Cu(II)-coordinated vs respective uncoordinated compound.
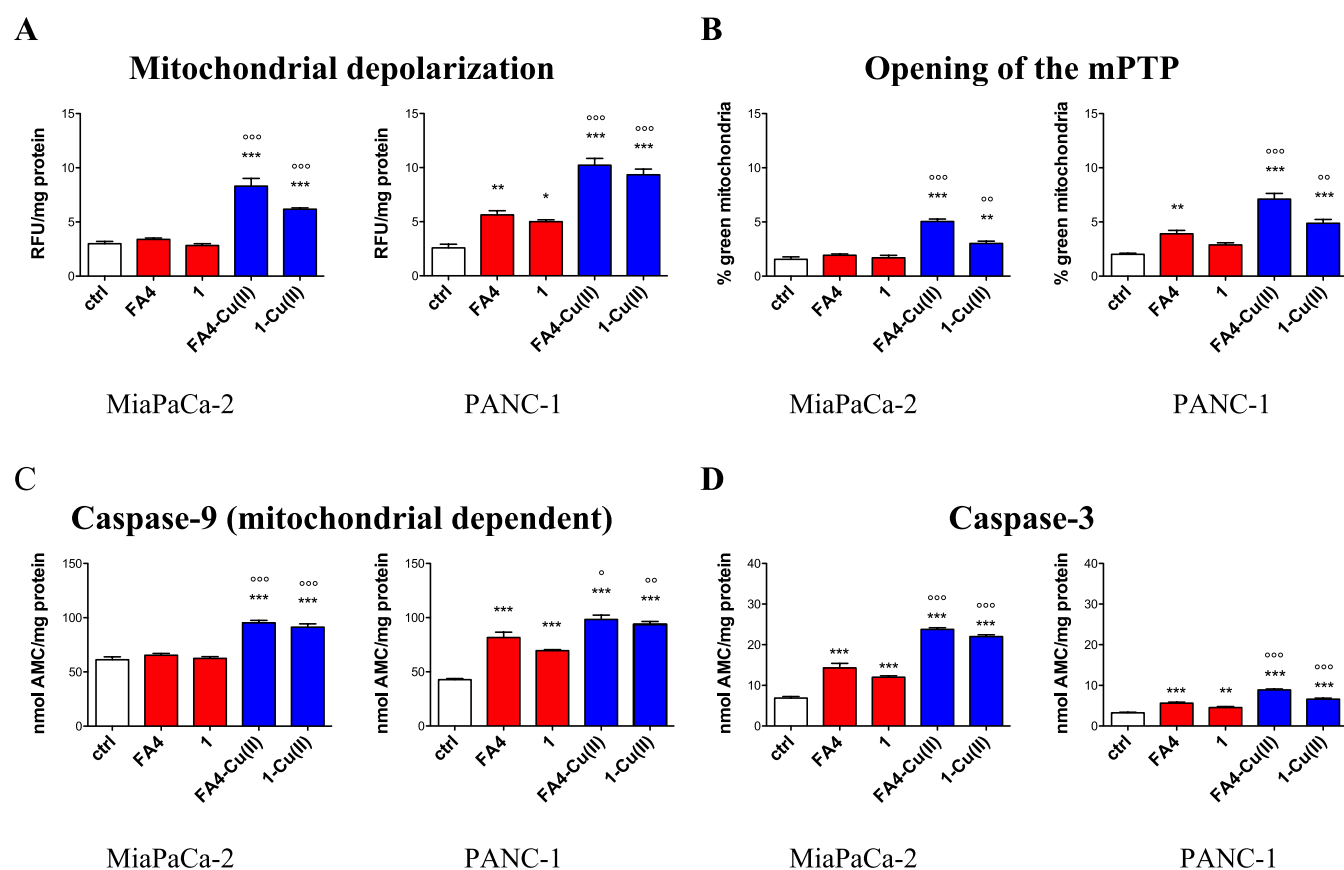
Figure 7. Mitochondrial depolarization (A), mPTP opening (B), and caspase 9 (C) and caspase 3 (D) activation in MiaPaCa-2 and PANC-1 cells treated with **FA4**, **1**, and their Cu(II) complexes for 24 h at 50 μM concentration. Data are means + SD ($n = 3$). *$p < 0.05$, **$p < 0.01$, ***$p < 0.001$ vs ctrl; °$p < 0.05$, °°$p < 0.01$, °°°$p < 0.001$: Cu(II)-coordinated vs respective uncoordinated compound.

A preliminary investigation of the ROS (reactive oxygen species) involvement in the cytotoxicity exerted by TSCs **1** and **FA4** and their Cu(II) and Pt(II) complexes was evaluated by coadministering the compounds with the antioxidant compound α-tocopherol (Figure 4).

While the effect of the administration of α-tocopherol with **1** was almost undetectable, because of the negligible cytotoxicity of **1** with the conditions of the assay (24 h), the cytotoxic action of **1**-Cu was not reverted by α-tocopherol, in both PANC-1 and MiaPaCa-2 cells. On the other hand, a drastic reversion of the activity was recorded in both cells treated with **FA4** and its Cu(II) complex (Figure 4A,B). Because of the higher EC_{50} values in MiaPaCa-2 and PANC-1 cells and the concentration of TSCs used, no changes in the antiproliferative activity of both **1** and **FA4**-Pt complexes were recorded upon cotreatment with α-tocopherol (Figure 4A,B). These results together show how copper complexation confers an increased antitumor activity and that the S2R-targeting portion can activate ROS-dependent death pathways both in the metal-free TSC and the TSC-Cu complex (i.e., **FA4** and **FA4**-Cu, respectively). In addition, these data highlight that S2R-targeting may engage pathways beyond copper complexation, linking the activity exerted through the target engagement, i.e., S2R, with the activity due to the copper chelation, thus deserving a more in-depth investigation.

ER Stress and ER-Dependent Apoptosis. According to the expression of ER stress sensors, we found that **1**, **FA4** and particularly their Cu(II) complexes, induce ER stress, as suggested by the increase in the expression of ER stress sensor GRP78, ATF6, IRA-1 and PERK (Figure 5A).[43]

Notably, the effects were more pronounced with the copper complexes and on PANC-1 than on MiaPaca-2 cells. This result is of particular interest because PANC-1 cells are more resistant to gemcitabine,[17] the first-line treatment used in pancreatic adenocarcinoma (PDAC) therapy. Hence, finding alternative pharmacological strategies against this resistant model is of paramount importance. We identified **FA4**, particularly **FA4**-Cu, as a potent anticancer agent, and we clarified that a possible mechanism can be mediated by the induction of ER stress. It has already been reported the localization of S2R in ER and its involvement in triggering ER stress.[44] The different sensitivity between the cell lines can be attributed to a different expression and activity of the ER quality control/ER-associated degradation (ERQC/ERAD) complex that makes cells less or more resistant to ER stress. Of note cells resistant to chemotherapy, such as PANC-1, have an active ERQC/ERAD complex that works at its maximal capability and is easily deranged by ER perturbers,[45] as TSC agents. Copper is a further inducer of ER stress, causing the upregulation of GRP78 and the consequent activation of PERK and ATF4.[46] This event is observed with our Cu(II) complexes, where the ER stress toxicity induced by TSC is enhanced by the presence of copper.

If ER stress is limited, cells activate pro-survival pathways, but the ERQC/ERAD system is unable to compensate ER stress and apoptotic cell death prevails.[43] The typical executer of ER stress-dependent apoptosis is caspase 7 that is indeed
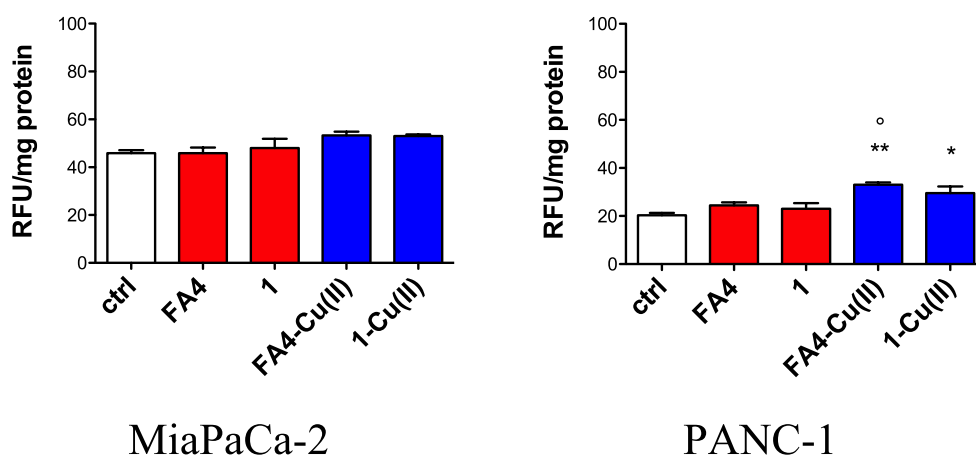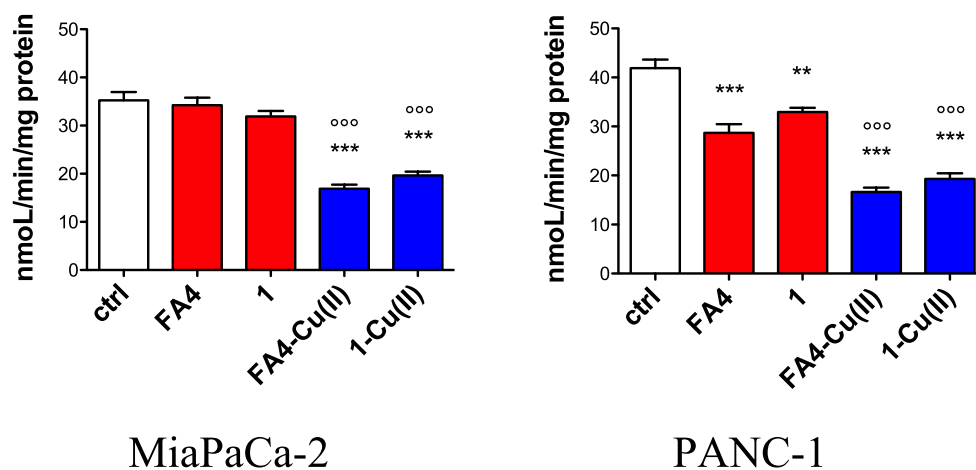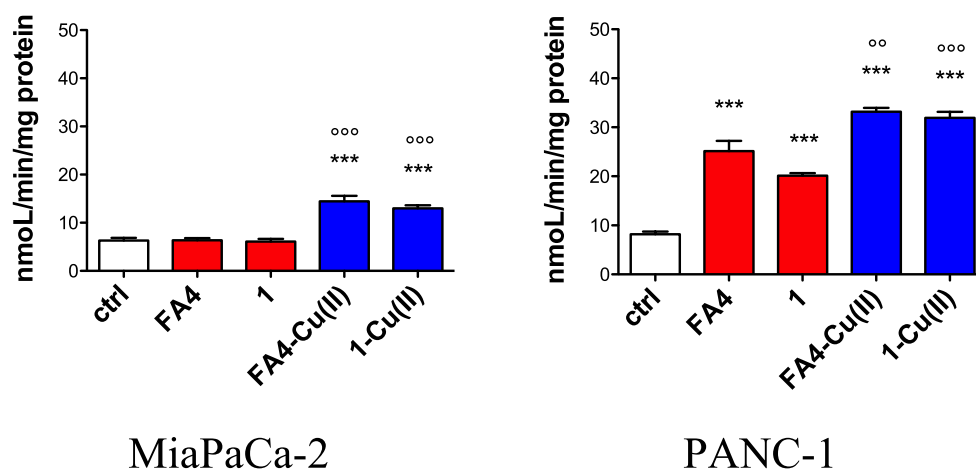
Figure 8. ROS (A), GSH (B), and GSSG (C) in the lysates of MiaPaCa-2 and PANC-1 cells treated with **FA4**, **1**, and their Cu(II) complexes for 24 h at a 50 μM concentration. Data are means + SD ($n = 3$). $*p < 0.05$, $**p < 0.01$, $***p < 0.001$ vs ctrl; $°p < 0.05$, $°°p < 0.01$, $°°°p < 0.001$: Cu(II)-coordinated vs respective uncoordinated compound.
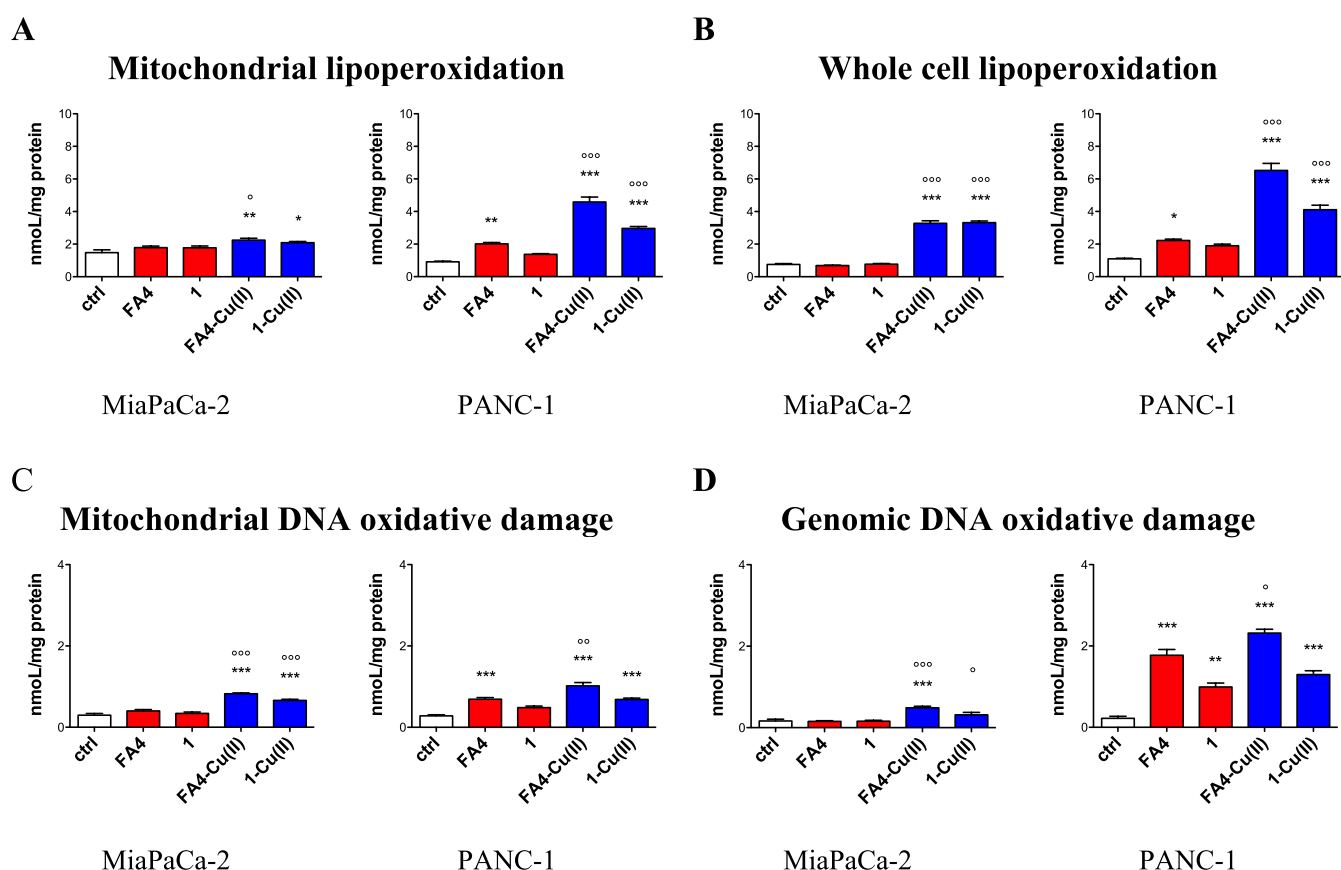
Figure 9. Lipoperoxidation in whole cell (A) and mitochondrial extracts (B), oxidative damage of genomic (C) and mitochondrial (D) DNA in MiaPaCa-2 and PANC-1 cells treated with **FA4**, **1**, and their Cu(II) complexes for 24 h at 50 μM concentration. Data are means + SD (n = 3). $*p < 0.05$, $**p < 0.01$, $***p < 0.001$ vs ctrl; $°p < 0.05$, $°°p < 0.01$, $°°°p < 0.001$: Cu(II)-coordinated vs respective uncoordinated compound.

activated by **1** and **FA4**, particularly by Cu(II) complexes, in line with the different extent of ER stress (Figure 5B).

Mitochondrial Stress and Mitochondrial-Dependent Apoptosis. CuSO$_4$ in liver cancer triggers apoptosis by impairing the mitochondrial functions and inducing oxidative stress,[46] in consequence of the perturbations of ER stress, which is in contact with the mitochondrial network, and influence the mitochondrial homeostasis.[47] Indeed, mitochondrial-delivery systems of Cu have been recently developed as anticancer drugs,[48] opening the way to a new category of antitumor agents.

In line with this observation, the Cu(II) complexes of **1** and **FA4** reduced the efficacy of the electron transport chain (Figure 6A) and the consequent production of mitochondrial ATP (Figure 6B). The reduced efficiency of oxidative phosphorylation results in partial reduction of the O$_2$, with the generation of ROS. Indeed, the staining with MitoSOX, a fluorescent probe specific for mitochondrial ROS, indicated that the Cu(II) complexes increased the intramitochondrial level of ROS (Figure 6C).

ROS are known to induce peroxidation of membrane lipid of mitochondria, inducing the loss of membrane polarization and the opening of the mitochondria permeability transition pore (mPTP), coupled with a decrease in antioxidant enzymes as superoxide dismutase (SOD) and reduced glutathione (GSH).[49] In line with these findings, Cu(II) complexes induced the loss of mitochondrial potential, as indicated by JC1 staining (Figure 7A) and opening of mPTP (Figure 7B), followed by the activation of caspase 9 (Figure 7C), a typical

caspase activated in response to mitochondrial damage.[50] The concomitant activation of caspase 7 and caspase 9 ultimately led to the activation of caspase 3 (Figure 7D), the final executor of apoptotic death. The effect is particularly pronounced in PANC-1 cells, and this result is of translational relevance since it represents an effective strategy to kill highly chemoresistant cells.

ROS increased not only in the mitochondria but also in the entire cell following treatment with TSC-Cu (Figure 8A). Consistently, treated cells showed a decrease in reduced glutathione (GSH; Figure 8B) and an increase in oxidized glutathione (GSSG; Figure 8C), in agreement with GSH reactivity studies in solution (Figure 3). It is important to note that elevated GSH levels are associated with tumor progression and drug resistance, whereas decreasing GSH levels through oxidation to GSSG is a promising anticancer strategy.

Lipid Peroxidation and DNA Damage. The oxidative effects were more pronounced in PANC-1 cells, where compounds **1** and **FA4** also produced increased ROS and GSSG/GSH ratio than in MiaPaca-2, where only the Cu(II) complexes of **1** and **FA4** were active. This difference could be dependent on the different intrinsic activity of antioxidant enzymes. The activity of the mitochondrial Cu-dependent SOD2, which is increased in response to oxidative damage in PANC-1 cells, where the mitochondrial oxidative stress is higher, was increased by **1**-Cu and **FA4**-Cu and also by the TSC alone. By contrast, in MiaPaCa-2, where the oxidative stress was mild, the increase was achieved only by **1**-Cu and
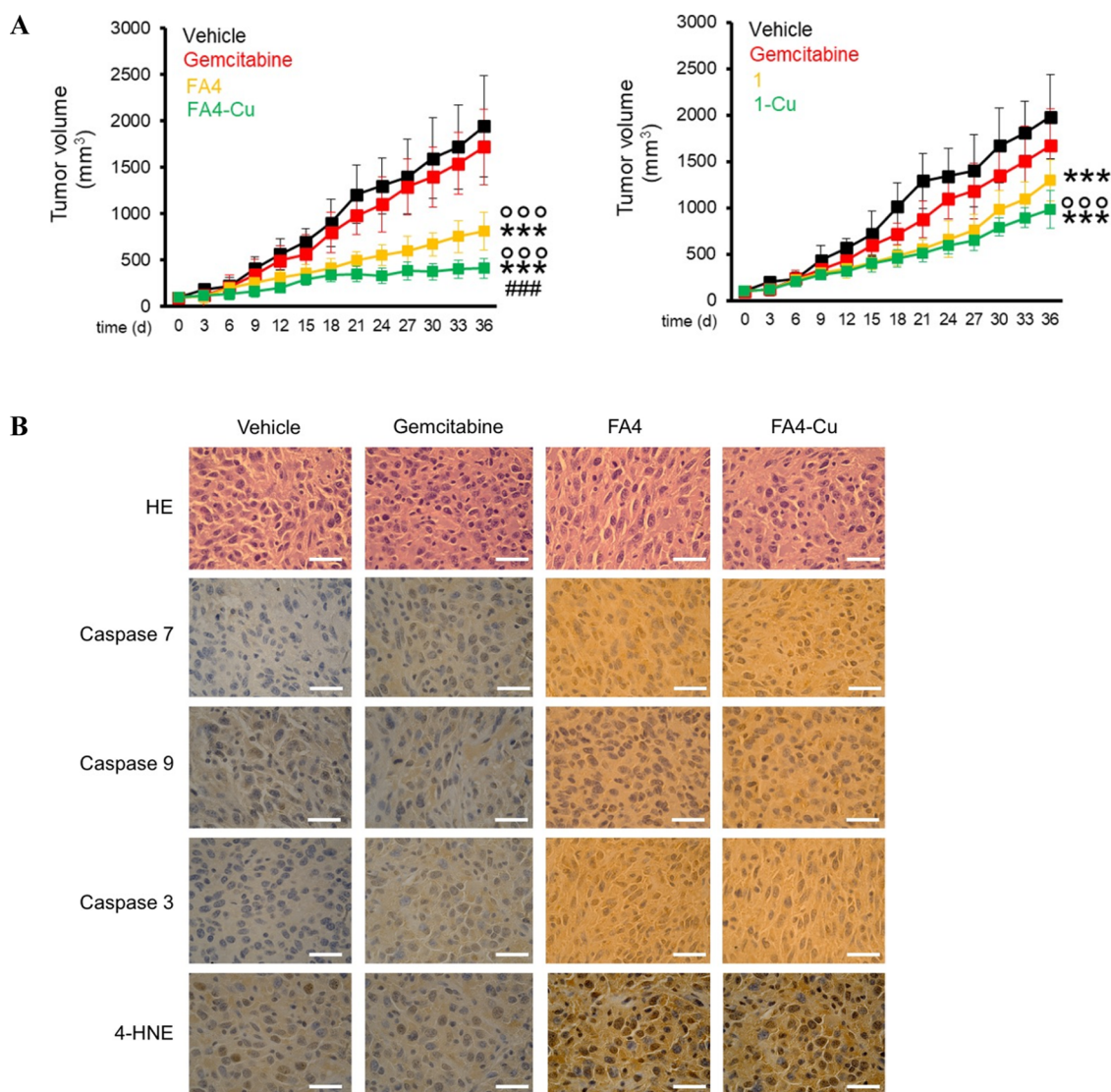
Figure 10. *In vivo* efficacy of FA4 and 1 and their Cu(II) complexes. (A) C57BL/6 mice were injected with 2×10^6 PANC-1 cells. When the tumor reached a volume of 100 mm^3, the animals were randomized into the following treatment groups ($n = 5$/group) and treated daily for 30 days as follows: (1) control group (vehicle), treated with 100 μL saline solution intraperitoneally (ip); (2) **FA4** or **1**, treated with 750 nmoles of the compound in 100 μL saline solution, ip; (3) **FA4**-Cu or **1**-Cu, treated with 750 nmoles compound in 100 μL of saline solution, ip; (4) gemcitabine, 20 mg/kg, administered twice a week, ip, as an internal control. Tumor growth was monitored using calipers, and animals were euthanized on day 36. ***: $p < 0.001$ vs vehicle; °°°: $p < 0.001$: **FA4**/**FA4**-Cu/**1**-Cu vs gemcitabile; ###: $p < 0.001$: **FA4**-Cu vs **FA4**. (B) Tumor sections were stained with hematoxylin and eosin (HE) or immunostained for Caspase 7, Caspase 9, Caspase 3, and 4-HNE (4-hydroxy-nonenal), a marker of oxidative stress targeting lipids. The image shown is representative of 1 out of 5 animals. Scale bars: 100 μm (10× ocular; 40× objective).

FA4-Cu, although at a lower extent (Figure S14A). The same trend was observed for cytosolic SOD1 (Figure S14B).

As a result of oxidative stress, the TSCs and particularly their Cu(II) complexes induce lipid peroxidation, as demonstrated by the increase in 9-OH-nonenal, an index of lipid peroxidation in both whole cells and mitochondrial extracts (Figure 9A,B) and oxidative damage of genomic and mitochondrial DNA (Figure 9C,D), indicated by the increase in 8-OH-deoxyguanosine.

In Vivo Antitumor Activity of 1 and FA4 and Their Cu(II) Complexes. The activity of TSCs **1** and **FA4** and the corresponding Cu(II) complexes was evaluated *in vivo* in a xenograft model of the pancreatic tumor of clinical significance, *i.e.*, the gemcitabine-resistant PANC-1 cells. All TSCs were administered daily at the concentration of 0.75 mmol/mL, corresponding to the lower effective concentration of **FA4** in

the same xenograft PANC-1 model[17] for 35 days. All TSCs were more potent than the standard treatment of Gemcitabine (Figure 10A, right and left panel). **FA4**-Cu and **1**-Cu had a superior activity than **FA4** and **1**, respectively, recapitulating, *in vivo*, the superior activity of the complexes highlighted *in vitro*, in terms of EC$_{50}$ values, caspase 7, caspase 9, and caspase 3 activation, and lipid peroxidation (Figure 10B). Of note, **FA4** and its Cu(II) complex **FA4**-Cu (Figure 10A, right panel) were more active than **1** and its Cu(II) complex **1**-Cu (Figure 10A, left panel), suggesting how the S2R-targeting moiety confers a more potent effect. **FA4**-Cu emerged as the most potent compound, with a promising profile, as evidenced by the lack of alterations in weight (Supporting Figure S15), post-mortem hematochemical parameters (Table S2), and in histopathology of the liver, kidneys, and spleen (Figure S16). The lack of

toxicity *in vivo* was in line with the lack of cytotoxicity on nontumoral pancreatic epithelial cells observed *in vitro*.

CONCLUSIONS

The incidence of pancreatic cancer continues to increase with the lowest 5-year survival rate, and it is predicted to become the second leading cause of cancer-related deaths by 2030.[51,52] Clinical trials with novel therapeutic regimens have not shown better outcomes compared to first-line treatment with gemcitabine alone.[53] Therefore, there is an urgent need for novel therapies to overcome the paucity and poor efficacy of the current regimens, to which patients often develop resistance. S2R-targeting TSCs were developed with this perspective. Leveraging (i) S2R overexpression and mediated activity in pancreatic tumors, (ii) FA4's strong cytotoxic activity against pancreatic cancer in a preclinical model; and (iii) TSCs' ability to chelate divalent metal ions of therapeutic significance, we developed and validated Cu(II) and Pt(II)-FA4 complexes targeting S2R, and compared them with the corresponding TSC complex that does not bind S2R (*i.e.*, **1**). The cytotoxicity of compounds increases in the order **1**-Pt/FA4 < **1**/FA4 < **1**-Cu/FA4, indicating that, while the Cu(II) ion contributes to enhancing cytotoxic effects, Pt(II) diminishes this effect, despite similar stoichiometry and coordination geometry of the two metal complexes. This is attributed to the lower propensity of the Pt(II) complex for ligand exchange and transmetalation, as well as its scarce ability to trigger redox reactions, in contrast to the Cu(II) complex, which shows reactivity with GSH and the ability to form GSSG. The findings also suggest that the Pt(II) complex with **1**/FA4 exhibits less affinity for binding DNA and inducing apoptosis compared to another monofunctional Pt(II) complex, such as phenanthriplatin.

Considering that Cu(II)-TSCs were much more active than their Pt(II) counterparts *in vitro*, **FA4**-Cu mechanisms of action were thoroughly investigated in PANC-1 and MiaPaCa-2 cells and compared with **1**-Cu. The activity of the copper complexes in these cells was also compared with that of the copper-free TSCs. **FA4**-Cu induced apoptotic cell death through ER stress and mitochondria disfunction. PANC-1 cells, with clinical relevance, were more sensitive to the mechanisms activated by TSCs and particularly by **FA4** with enhanced activity observed with **FA4**-Cu. The promising *in vitro* results were replicated in a preclinical xenograft model of PANC-1 cancer, where **FA4**-Cu was the most potent compound, performing slightly better than its metal-free counterpart, **FA4**. All TSCs (copper-coordinating and copper-free) outperformed gemcitabine and were safe, showing no signs of hematological or organ toxicity. The activity of the S2R-targeting TSCs was stronger than that of compound **1**, which lacks the S2R-targeting moiety, thus corroborating the beneficial synergistic anticancer activity of TSCs and their copper complexes. The encouraging results obtained with **FA4**-Cu in this very aggressive form of pancreatic tumor strongly support further studies to explore its potential as a therapeutic agent.

EXPERIMENTAL SECTION

Chemistry. All chemicals, unless otherwise stated, were purchased from Sigma-Aldrich, TCI Chemicals, Alfa Aesar, or Acros Organics. Thin layer chromatography (TLC) was performed by using plates from Merck (silica gel 60 F254). Column chromatography was performed with 60 Å of Merck silica gel (63−200 mm) as the stationary phase. Melting points were determined in open capillaries on a Gallenkamp electrothermal apparatus. All spectra were in accordance with the assigned structures. Electrospray ionization mass spectrometry (ESI-MS) was performed with a dual electrospray interface and a quadrupole time-of-flight mass spectrometer (Agilent 6530 Series Accurate-Mass Quadrupole Time-of-Flight (Q-TOF) LC-MS) (Agilent Technologies Italia S.p.A.; Cernusco sul Naviglio, Milano, Italy). 1D ^1H, ^{13}C, and ^{195}PtNMR spectra and 2D [^1H−^{13}C]-HSQC and [^1H−^{13}C]-HMBC spectra were recorded on An Agilent Technologies 500 MHz instrument. The internal residual peak of the solvent was used to calibrate 1D ^1H and ^{13}C NMR spectra (DMF-d_7: 8.03 ppm for ^1H and 163.15 ppm for ^{13}C; methanol-d_4: 3.31 ppm for ^1H and 49.15 ppm for ^{13}C). ^{195}Pt chemical shifts were referenced to external $K_2[PtCl_4]$ in D_2O fixed at −1628 ppm. Elemental analyses were performed with a Eurovector EA 3000 CHN instrument (Eurovector S.p. A., Milano, Italy). UV−vis spectra were recorded on a Hewlett-Packard 8452A spectrophotometer equipped with a circulation thermostat Infrared spectra were recorded in the wavelength range from 4000 to 200 cm^{-1} with a spectral resolution of 2 cm^{-1} using a PerkinElmer Spectrum One FTIR spectrometer. The samples were prepared with the KBr pellet method.

Purity for all compounds is >95% by elemental analysis.

Synthesis of [CuCl(ACthio-1)] (1-Cu). **1** (40 mg, 0.16 mmol) was dissolved in EtOH (7.5 mL) at 40 °C and treated with an equimolar amount of $CuCl_2$ (21.7 mg, 0.16 mmol). The resulting mixture was stirred overnight at 40 °C. The brown solid that precipitated was isolated by filtration, washed with Et_2O, and dried under a vacuum. Obtained 43.02 mg (77.2% yield). Anal. Calcd for [CuCl(ACthio-1)] ($C_{11}H_{11}ON_4SCuCl$): C, 38.15; H, 3.20; N 16.18%. Found: C, 38.49; H, 2.96; N, 16.08%. ESI-MS(−): calcd for $[C_{11}H_{11}ON_4SCuCl − H]^-$ m/z = 343.9659; found: $[M − H]^-$ m/z = 343.2835.

Synthesis of [CuCl(FA4)] (FA4-Cu). **FA4**·HCl (25 mg, 0.047 mmol) was dissolved in EtOH (15 mL) at 40 °C and treated with an equimolar amount of $CuCl_2$ (6.36 mg, 0.047 mmol). The resulting mixture was stirred overnight at 40 °C. The dark-gold solid that precipitated was filtered, washed with Et_2O, and dried under a vacuum. Obtained: 19.4 mg (66.0% yield). Anal. Calcd for [CuCl(FA4)] ($C_{27}H_{32}O_2N_5SCuCl·HCl$): C, 51.80; H, 5.31; N 11.19%. Found: C, 51.50; H, 5.61; N, 11.12%. ESI-MS(+): calcd for $[C_{27}H_{32}O_2N_5SCuCl + H]^+$ m/z = 589.1439; found: $[M + H]^+$ m/z = 589.1329.

Synthesis of [PtCl$_2$(DMSO)$_2$]. Complex [$PtCl_2(DMSO)_2$] was prepared according to a previously reported procedure.[54] The characterization of the compound provided data in accordance with those reported in the literature.

Preparation of [PtCl(1)] (1-Pt). **1** (20 mg, 0.081 mmol) was dissolved in MeOH (20 mL) at 40 °C and treated with [$PtCl_2(DMSO)_2$] (34.01 mg, 0.081 mmol). The resulting mixture was stirred at 40 °C for 24 h. The dark-brown solid that precipitated was filtered, washed with Et_2O, and dried under a vacuum. Obtained: 21.7 mg (56.1% yield). Anal. Calcd for [PtCl(ACthio-1)]·2H$_2$O ($C_{11}H_{11}ON_4SPtCl·2H_2O$) C, 25.71; H, 2.94; N 10.90%. Found: C, 25.69; H, 2.42; N, 10.95%. ESI-MS(−): calcd for $[C_{11}H_{11}ON_4SPtCl − H]^-$ m/z = 476.9863; found: $[M − H]^-$ m/z = 476.9909. ^1H NMR (DMF-d_7): 12.25 (1H, N$_2$H), 7.71 (1H, H$_4$), 7.45 (1H, H$_5$), 7.18 (1H, H$_6$), 7.11 (1H, H$_7$), 3.70 (3H, H$_{14}$), 3.50 (3H, H$_{15}$) ppm. ^{13}C NMR (DMF-d_7): 192.37 (C$_{12}$), 184.54 (C$_1$), 145.87 (C$_3$), 142.15 (C$_9$), 132.36 (C$_5$), 126.06 (C$_4$), 125.27 (C$_6$), 118.02 (C$_8$), 114.61 (C$_7$), 43.50 (C$_{15}$), 40.70 (C$_{14}$) ppm.

Synthesis of [Pt(FA4)Cl] (FA4-Pt). **FA4**·HCl (15 mg, 0.026 mmol) was dissolved in MeOH (15 mL) at 40 °C and treated with [$PtCl_2(DMSO)_2$] (11.20 mg, 0.026 mmol). The resulting mixture was stirred at 40 °C for 24 h. The obtained solution was concentrated to a minimum volume, and Et_2O was added to induce precipitation of the desired product as a dark-brown solid. The precipitate was isolated by filtration, washed with Et_2O, and dried under a vacuum. Obtained 17.5 mg (88.8% yield). Anal. Calcd for [PtCl(FA4)]·HCl·2H$_2$O ($C_{27}H_{32}O_2N_5SPtCl·HCl·2H_2O$): C, 40.88; H, 4.71; N 9.10%. Found: C, 40.86; H, 4.69; N, 8.82%. ESI-MS(+): calcd for $[C_{27}H_{32}O_2N_5SPtCl + H]^+$ m/z = 722.1637; found: $[M + H]^+$ m/z

= 722.1674. ^{1}H NMR (MeOD-d_4): 7.62 (1H, H$_4$), 7.46 (1H, H$_5$), 7.33 (2H, H$_{30,31}$), 7.29 (2H, H$_{29,32}$), 7.18 (2H, H$_{6,7}$), 5.10 (1H, H$_{26}$), 3.97 (1H, H$_{16}$), 3.63 (1H, H$_{21,25}$), 3.56 (3H, H$_{15}$), 3.41 (1H, H$_{21,25}$), 3.31 (3H, H$_{14}$), 2.25 (1H, H$_{22,24}$), 1.98 (1H, H$_{22,24}$), 1.92 (2H, H$_{17,18}$) ppm. ^{13}C NMR (MeOD-d_4): 193.40 (C$_{12}$), 183.47 (C$_1$), 146.09 (C$_3$), 144.40 (C$_{27}$), 141.14 (C$_9$), 140.38 (C$_{28}$), 132.24 (C$_5$), 129.79 (C$_{30}$), 128.99 (C$_{31}$), 126.21 (C$_4$), 126.00 (C$_6$), 122.69 (C$_{29}$), 121.75 (C$_{32}$), 117.98 (C$_8$), 113.31 (C$_7$), 83.12 (C$_{23}$), 72.38 (C$_{26}$), 57.78 (C$_{19}$), 51.50 (C$_{21,25}$), 44.01 (C$_{15}$), 41.26 (C$_{16}$), 41.00 (C$_{14}$), 35.11 (C$_{22,24}$), 25.91 (C$_{18}$), 22.37 (C$_{17}$).

X-ray Powder Diffraction. *X-ray Crystallographic Data Collection and Structure Refinement for Copper(II) Complex of (Z)-2-(1-(4-(3H-Spiro[isobenzofuran-1,4'-piperidine]-1'-yl)butyl)-2-oxoindolin-3-ylidene)-N,N-dimethylhydrazinecarbothioamide (FA4-Cu).*[55] Crystallographic studies of structural characterization of **FA4** compound was performed by using a Rigaku Rint2500 laboratory diffractometer with a rotating copper anode. The instrument operated at 50 kV and 200 mA in a Debye−Scherrer geometry. The diffractometer is equipped with an asymmetric Johansson Ge (111) crystal to select the monochromatic Cu Kα_1 radiation (λ = 1.54056 Å) along with the silicon strip Rigaku D/teX Ultra detector. The data were collected in the range 6 to 80° (2ϑ) with a step size of 0.02° (2ϑ) and a counting time of 12 s/step. To perform the measurements, the powder sample was introduced in a glass capillary with a diameter of 0.5 mm and mounted on the goniometer's axis. The capillary was rotated during the measurement to enhance the randomization of the individual crystallites' orientations and minimize the potential impact of the preferred orientation.

The structure determination and refinement of **FA4**-Cu was automatically performed using EXPO software,[40] a package capable of the following steps: (a) determination of unit-cell parameters and identification of the space group; (b) structure solution *via* direct methods and/or a real-space approach; (c) structure model refinement using the Rietveld method.[56] The first low-angle, well-defined peaks in the experimental diffraction pattern were selected and actively used for indexing with N-TREOR09[57] and DICVOL04[58] programs embedded in EXPO. Space group determination was based on the evaluation of systematic absences.

The structure was solved with a real-space method based on the simulated annealing algorithm implemented in EXPO. The starting model was built using the sketching facilities of ACD/ChemSketch[59] and the geometry optimization was performed by the program MOPAC2016.[60] The simulated annealing algorithm was run 100 times under a Linux workstation in default mode and parallel calculation over 40 CPUs. The best solution with the lowest cost function value was selected. The criterion to accept the solution was also based on the soundness of the crystal packing.

The resulting structure was refined by the Rietveld method. Restraints were applied to bond distances and angles to stabilize the refinement. All H atoms bonded to C atoms were treated as riding atoms under the constraint of atomic displacement parameters U_{iso}(H) = 1.2U_{iso}(C). The peak shape was modeled using the Pearson VII function. Only six atomic displacement parameters were refined isotropically.

Reactivity with Glutathione and Transmetalation. The reactivity of **FA4** and its Cu(II) and Pt(II) complexes with GSH was investigated by using UV−vis spectroscopy. GSH was dissolved at a concentration of 3 mM in 100 mM HEPES buffer (pH 7.4) with 5% DMSO or DMF. **FA4** and its complexes with Cu(II) and Pt(II) were added at a concentration of 30 μM, corresponding to a 1:100 molar ratio with GSH. For anaerobic incubation, all solutions were deoxygenated and mixed under a nitrogen atmosphere. UV−vis spectra were acquired in the range of 250−600 nm.

The transmetalation of the Pt(II) complex in the presence of a Cu(II) salt was investigated by ESI-MS. For this purpose, **FA4**-Pt (2 mM) was incubated with an equimolar amount of CuCl$_2$ for 24 h in DMF. The mixture was then diluted with 50% MeOH, and an ESI-MS spectrum was recorded at the end of the incubation period.

Biology. *Cell Lines.* Human MiaPaCa-2, PANC-1 pancreatic ductal adenocarcinoma, and human pancreatic epithelial HPDE cell lines were obtained from American Type Culture Collection (ATCC, Bethesda, MD), and cultured in DMEM medium with 10% v/v fetal bovine serum (FBS) and 1% v/v penicillin-streptomycin, in a humidified incubator at 37 °C with 5% CO$_2$.

Cell Viability. The determination of cell growth was performed using the MTT assay at 48 and 72 h.[16] On day 1, 25,000 cells/well were seeded into 96-well plates in a volume of 100 μL. At day 2, the various drug concentrations (0.1 to 100 μM) were added. In all of the experiments, the various drug solvents (EtOH, DMSO) were added in each control to evaluate a possible solvent cytotoxicity. After the established incubation time with drugs (48 h), MTT (0.5 mg/mL) was added to each well, and after 3−4 h of incubation at 37 °C, the supernatant was removed. The formazan crystals were solubilized using 100 μL of DMSO/EtOH (1:1) and the absorbance values at 570 and 630 nm were determined on the microplate reader Victor 3 from PerkinElmer Life Sciences. The interference of ROS in cell viability was indirectly determined by the MTT assay reported above at 24 h. On day 1, 25,000 cells per well were seeded into 96-well plates in the presence or absence of α-tocopherol (100 μM). On day 2, the drugs (1, 5, 10 μM) were added alone and in combination with α-tocopherol (100 μM). After incubation (24 h) with drugs, the MTT assay was performed as above.

Real-Time PCR. One microgram total RNA was reverse transcribed using the iScript Reverse Transcription Supermix kit (Bio-Rad Laboratories), according to the manufacturer's instruction. Twenty-five ng cDNA were amplified with 10 μL IQTM SYBR Green Supermix (Bio-Rad Laboratories). Primers were designed with the qPrimer Depot software (http://primerdepot.nci.nih.gov/). qRT-PCR was carried out with a CFX96 Real-Time Detector System (Bio-Rad Laboratories). Cycling conditions were: 30 s at 95 °C, followed by 40 cycles of denaturation (15 s at 95 °C), annealing/extension (30 s at 60 °C). The same cDNA preparation was used to quantify the genes of interest, and the housekeeping gene *S14*, used to normalize gene expression. The relative quantitation of each sample was performed using the Gene Expression Quantitation software (Bio-Rad Laboratories). Results were expressed in arbitrary units. For each gene, the expression in untreated cells was considered "1".

Caspase Activation. Caspase 3, Caspase 7, and Caspase 9 activation were measured by using the Caspase 3/7 Fluorescence Assay kit (Cayman Chemical, Ann Arbor, MI) and the Caspase 9 fluorimetric assay kit (Enzo Life Science, Roma, Italy). The results are expressed as nanomoles of the hydrolyzed substrate of each caspase/mg cellular proteins, according to a previously set titration curve.

Mitochondrial Extraction, Electron Transport Chain (ETC), and ATP. Mitochondrial extracts and energetic parameters were measured as detailed in the literature.[61] Cells were washed twice in ice-cold PBS, lysed in 0.5 mL mitochondria lysis buffer (50 mmol/L Tris, 100 mmol/L KCl, 5 mmol/L MgCl$_2$, 1.8 mmol/L ATP, 1 mmol/L EDTA, pH 7.2), supplemented with protease inhibitor cocktail III (Merck), 1 mmol/L PMSF and 250 mmol/L NaF. The samples were clarified by centrifugation at 650g for 3 min at +4 °C: the supernatant was collected and centrifuged at 13,000g for 5 min at +4 °C; the pellet containing mitochondria was washed once with lysis buffer and resuspended in 0.25 mL of a resuspension buffer composed of 250 mmol/L sucrose, 15 mmol/L K$_2$HPO$_4$, 2 mmol/L MgCl$_2$, 0.5 mmol/L EDTA. A 50 μL aliquot was sonicated and used for the measurement of protein content. To measure the electron flux from complex I to complex III, taken as index of the mitochondrial respiratory activity, 50 μg of nonsonicated mitochondrial samples were resuspended in 0.2 mL of buffer A (5 mmol/L KH$_2$PO$_4$, 5 mmol/L MgCl$_2$, 5% w/v BSA) and transferred into a quartz spectrophotometer cuvette. Then 0.1 mL of buffer B (25% w/v saponin, 50 mmol/L KH$_2$PO$_4$, 5 mmol/L MgCl$_2$, 5% w/v BSA, 0.12 mmol/L cytochrome c-oxidized form, and 0.2 mmol/L NaN$_3$) was added for 5 min at room temperature. The reaction was started with 0.15 mmol/L NADH and was followed for 5 min, reading the absorbance at 550 nm by a Packard microplate reader EL340 (Bio-Tek Instruments, Winooski, VT). The results were expressed as nanomoles of cytochrome c reduced/min (dABs)/mg mitochondrial protein. The amount of ATP in mitochondrial extracts was measured

with the ATP Bioluminescence Assay Kit (Sigma-Aldrich). The results were expressed as nmol/mg mitochondrial proteins.

Mitochondrial Depolarization. Staining with JC1 fluorescent probe (Biotium Inc., Freemont, CA) was performed as detailed.[62] The fluorescence units were used to calculate the percentage of green-fluorescent (i.e., depolarized) mitochondria versus red-fluorescent (i.e., polarized) mitochondria.

Mitochondrial Permeability Transition Pore (mPTP) Opening. The opening of the mPTP, an index of mitochondria depolarization and damage, was measured with the Mitochondrial Permeability Transition Pore Assay Kit (BioVision, Milpitas, CA), as per manufacturer's instructions, using a Guava EasyCyte (Millipore), equipped with the InCyte software (Millipore). Unstained cells (1×10^5) were used to set the threshold of autofluorescence and subtracted from the stained cells. Results were expressed as the percentage of fluorescent cells.

Reactive Oxygen Species (ROS). Intramitochondrial ROS was measured using the fluorescent probe MitoSOX (Invitrogen), as per the manufacturer's instruction. For total ROS, cells were incubated with 5 μmol/L of 5-(and-6)-chloromethyl-20,70-dichlorodihydro-fluorescein diacetate-acetoxymethyl ester (DCFDA-AM), as described.[62] The results are expressed as relative fluorescence units (RLUs) per milligram of mitochondrial or cellular proteins, respectively.

Reduced and Oxidized Glutathione (GSH and GSSG). Total, reduced (GSH) and oxidized (GSSG) glutathione content was measured by a colorimetric method, using a Packard microplate reader EL340 (Bio-Tek Instruments), as detailed previously[63] 1×10^5 cells were washed with 480 μL PBS, proteins were precipitated by adding 120 μL of 6.5% w/v 5-sulfosalicylic acid. Each sample was placed in ice for 1 h and centrifuged for 15 min at 13,000g (4 °C). Total glutathione was measured in 20 μL of the lysate with the following reaction mix: 20 μL stock buffer (143 mmol/L NaH$_2$PO$_4$ and 63 mmol/L EDTA, pH 7.4), 200 μL daily reagent (10 mmol/L 5,5′dithiobis-2-nitrobenzoic acid and 2 mmol/L NADPH in stock buffer), 40 μL glutathione reductase (8.5 U/mL). The content of oxidized glutathione (GSSG) was obtained after derivatization of GSH with 2-vinylpyridine (2VP): 10 μL of 2VP was added to 200 μL of lysate, and the mixture was shaken at room temperature for 1 h. Glutathione was then measured in 40 μL of the sample as described. The reaction was followed kinetically for 5 min using a Synergy HT Multi-Mode Microplate Reader (Bio-Tek Instruments, Vinooski, VT), measuring the absorbance at 415 nm. Each measurement was made in triplicate, and results were expressed as nanomoles glutathione/min/mg cell proteins. For each sample, reduced glutathione (GSH) was obtained by subtracting GSSG from the total glutathione. Results were expressed as nmoles of glutathione/min/mg cell proteins. For each sample, GSH was obtained by subtracting GSSG from total glutathione.

Superoxide Dismutase (SOD) Activity. Cytosolic SOD1 and mitochondrial SOD2 activity was measured using 10 μg of cytosolic and mitochondrial extract, respectively, incubated with 50 μmol/L xanthine, 5 U/mL xanthine oxidase, and 1 μg/mL oxidized cytochrome c. The rate of cytochrome c reduction, which is inhibited by the presence of SOD, was monitored for 5 min by reading the absorbance at 550 nm with a Packard microplate reader EL340 (Bio-Tek Instruments). Results, calculated as μmoles reduced cytochrome c/min/mg cytosolic or mitochondrial proteins corresponded to mU enzyme/mg proteins.

Lipoperoxidation Measurement. Lipoperoxidation was measured in whole cells and mitochondrial extracts by using the Lipid Peroxidation (4-HNE) Assay Kit (ab238538; Abcam, United Kingdom). Results were expressed as nanomoles per milligram of cell or mitochondrial proteins.

Oxidative DNA Damage. The amounts of oxidized genomic and mitochondrial DNA were measured in whole-cell extracts and mitochondrial extracts with the 8-hydroxy 2 deoxyguanosine ELISA Kit (Abcam). Results were expressed as nanomoles per milligram of genomic or mitochondrial DNA.

In Vivo Experiments. 2×10^6 PANC-1 cells were inoculated subcutaneously in the right flank of 6-week-old female nude mice (Species: *Mus musculus*; strain: C57BL/6, strain code: 027 from Charles River Laboratories Italia, Calco; total number of animals: 40), housed (5 per cage) under 12 h light/dark cycle, with food and drinking provided ad libitum. Tumor growth was measured daily by caliper according to the equation ($L \times W2)/2$, where L = tumor length and W = tumor width. When the tumor reached a volume of 100 mm³, mice (n = 5/group) were randomized in the following groups and treated daily for 30 days intraperitoneally as reported: (1) Vehicle group (100 μL saline solution containing 0.1% DMSO); (2) **FA4** or **1** (750 nmoles **FA4** or **1** in 100 μL saline solution containing 0.1% DMSO, corresponding to 19.8 mg/kg for **FA4** and 9.3 mg/kg for **1**); (3) **FA4**-Cu or **1**-Cu (750 nmoles **FA4**-Cu or **1**-Cu in 100 μL saline solution containing 0.1% DMSO, corresponding to 23.5 mg/kg for **FA4**-Cu and 12.9 mg/kg for **1**-Cu); (4) Gemcitabine group (20 mg/kg gemcitabine, twice a week). Tumor volumes and animal weight were monitored daily. Animals were euthanized on day 36 after randomization with zolazepam (0.2 mL/kg) and xylazine (16 mg/kg). Tumors were excised and paraffin-embedded. Sections were immunostained for cleaved caspase 7 (Antibodies.com), cleaved caspase 9 (Antibodies.com), cleaved caspase 3 (Cell Signaling Technology, Danvers, MA) or with anti-4-hydroxynonenal (Bioss) antibody, followed by a peroxidase-conjugated secondary antibody (Dako, Glostrup, Denmark). The sections were examined with a Leica DC100 microscope (Leica, Wetzlar, Germany). The liver, kidneys, and spleen were excised and paraffin-embedded, and the sections were stained with hematoxylin-eosin to observe the histology. Red blood cell (RBC) count, hemoglobin (Hb), white blood cells (WBC) count, platelets (PLT) count, lactate dehydrogenase (LDH), aspartate aminotransferase (AST), alanine aminotransferase (ALT), alkaline phosphatase (AP), creatinine, creatine phosphokinase (CPK), and cardiac troponin (c-TNT) were measured on blood samples collected immediately after euthanasia, using commercially available kits from Beckman Coulter Inc. (Beckman Coulter, Miami, FL). In all studies, researchers analyzing the results were unaware of the treatments received by the animals. The study complied with ARRIVE and IACUC guidelines. The animal experimental protocol was approved by the Ethical Committee of University of Torino and the Italian Ministry of Health (#254/2020-PR).

Statistical Analysis. Data were analyzed by applying the one-way repeated measures analysis of variance, and Bonferroni's multiple comparison test followed as a post hoc test. Results are reported as mean $\pm$ SD of at least two to three independent experiments, performed in triplicate. Statistical significance was accepted at $P <$ 0.05.

■ ASSOCIATED CONTENT

ⓈⒾ Supporting Information

The Supporting Information is available free of charge at https://pubs.acs.org/doi/10.1021/acs.jmedchem.4c01410.

> ESI-MS spectrum of **1**-Cu in DMF; proposed structure for **1**-Cu; overlay of absorption spectra recorded on a solution of **1** in DMSO during titration with CuCl$_2$; FTIR spectra of **1** and **1**-Cu; ESI-MS spectrum of **1**-Pt in DMF; 1D ^{13}C NMR spectra of free **1** and **1**-Pt in DMF-d_7; 1D ^{195}Pt NMR spectrum of **1**-Pt in DMF-d_7; 2D [^{1}H−^{13}C] HMBC NMR spectra of free **1** and **1**-Pt in DMF-d_7; ESI-MS spectrum of **FA4**-Cu in ethanol; proposed structure for **FA4**-Cu; overlay of absorption spectra recorded on a solution of **FA4** in DMSO during titration with CuCl$_2$; FTIR spectra of **FA4** and **FA4**-Cu; crystal packing of **FA4**-Cu molecules; ESI-MS spectrum of **FA4**-Pt in methanol; 1D ^{13}C NMR spectra of free **FA4** and **FA4**-Pt in methanol-d_4; 1D ^{195}Pt NMR spectrum of **FA4**-Pt in methanol-d_4; 2D [^{1}H−^{13}C] HSQC NMR spectra of free **FA4** and **FA4**-Pt in

methanol-d_4; 2D [^{1}H−^{13}C] HMBC NMR spectra of free **FA4** and **FA4**-Pt in methanol-d_4; time-dependent UV−vis spectra for the indicated reaction mixtures incubated under anaerobic conditions followed by oxygen exposure, and under direct aerobic conditions; time-dependent absorbance changes at 354 nm (λ_{max} of **FA4**) and 422 nm (λ_{max} of **FA4**-Cu and **FA4**-Pt), monitored by UV−vis spectroscopy, for the indicated reaction mixtures incubated under anaerobic conditions followed by oxygen exposure, and under direct aerobic conditions; ESI-MS spectra of **FA4**-Pt incubated with CuCl$_2$ for 24 h, recorded in positive (+) and negative (−) ion modes in DMF/MeOH (50%/50%); effect of TSCs **FA4**-Cu and **1**-Cu on mitochondrial Cu-containing enzyme SOD2 and cytosolic Cu-containing enzyme SOD1; weight of the animals, treated as in Figure 10 (n = 5 animals/group of treatment); histopathology of mice liver, kidney and spleen after treatment with **FA4** and **FA4**-Cu; X-ray powder diffraction data parameters and refinement statistics for **FA4**-Cu, and hematochemical parameters in mice measured immediately after euthanasia (PDF)

Smiles data (CSV)

AUTHOR INFORMATION

Corresponding Authors

Chiara Riganti − *Department of Oncology, Molecular Biotechnology Center "Guido Tarone", 10126 Torino, Italy;* orcid.org/0000-0001-9787-4836; Phone: +39-011-6705857; Email: chiara.riganti@unito.it

Carmen Abate − *Department of Pharmacy-Pharmaceutical Sciences, University of Bari Aldo Moro, 70125 Bari, Italy; Institute of Crystallography—CNR, 70126 Bari, Italy;* orcid.org/0000-0001-9292-884X; Phone: +39-080-5442727; Email: carmen.abate@uniba.it

Authors

Alessandra Barbanente − *Department of Chemistry, University of Bari Aldo Moro, 70125 Bari, Italy*

Joanna Kopecka − *Department of Oncology, Molecular Biotechnology Center "Guido Tarone", 10126 Torino, Italy*

Daniele Vitone − *Department of Chemistry, University of Bari Aldo Moro, 70125 Bari, Italy*

Mauro Niso − *Department of Pharmacy-Pharmaceutical Sciences, University of Bari Aldo Moro, 70125 Bari, Italy*

Rosanna Rizzi − *Institute of Crystallography—CNR, 70126 Bari, Italy*

Corrado Cuocci − *Institute of Crystallography—CNR, 70126 Bari, Italy*

Francesca Serena Abatematteo − *Department of Pharmacy-Pharmaceutical Sciences, University of Bari Aldo Moro, 70125 Bari, Italy*

Francesco Mastropasqua − *Department of Pharmacy-Pharmaceutical Sciences, University of Bari Aldo Moro, 70125 Bari, Italy*

Nicola Antonio Colabufo − *Department of Pharmacy-Pharmaceutical Sciences, University of Bari Aldo Moro, 70125 Bari, Italy;* orcid.org/0000-0001-5639-7746

Nicola Margiotta − *Department of Chemistry, University of Bari Aldo Moro, 70125 Bari, Italy;* orcid.org/0000-0003-4034-875X

Fabio Arnesano − *Department of Chemistry, University of Bari Aldo Moro, 70125 Bari, Italy;* orcid.org/0000-0002-8399-0964

Complete contact information is available at:
https://pubs.acs.org/10.1021/acs.jmedchem.4c01410

Author Contributions

#Equally contributing authors.

Notes

The authors declare no competing financial interest.

ABBREVIATIONS USED

(AD)Alzheimer's disease; (CNS)central nervous system; (DMF)dimethylformamide; (ER)endoplasmic reticulum; (ESI-MS)electrospray mass spectrometry; (GEM)gemcitabine; (GSH)reduced glutathione; (GSSG)oxidized glutathione; (LDL)low-density lipoprotein; (MeOH)methanol; (mPTP) mitochondria permeability transition pore; (NMR)nuclear magnetic resonance; (PGRMC1)progesterone receptor component 1; (ROS)reactive oxygen species; (S2R)sigma-2 receptor; (SOD)superoxide dismutase; (TMEM97)transmembrane protein 97; (TSPO)translocator protein; (TSCs) thiosemicarbazones; (XRPD)X-ray powder diffraction

REFERENCES

(1) Schmidt, H. R.; Kruse, A. C. The Molecular Function of σ Receptors: Past, Present, and Future. *Trends Pharmacol. Sci.* **2019**, *40*, 636−654.

(2) Abatematteo, F. S.; Niso, M.; Lacivita, E.; Abate, C. σ2 Receptor and Its Role in Cancer with Focus on a MultiTarget Directed Ligand (MTDL) Approach. *Molecules* **2021**, *26*, No. 3743.

(3) Zeng, C.; Riad, A.; Mach, R. H. The Biological Function of Sigma-2 Receptor/TMEM97 and Its Utility in PET Imaging Studies in Cancer. *Cancers* **2020**, *12*, No. 1877.

(4) Liu, C. Z.; Mottinelli, M.; Nicholson, H. E.; McVeigh, B. M.; Wong, N. K.; McCurdy, C. R.; Bowen, W. D. Identification and characterization of MAM03055A: A novel bivalent sigma-2 receptor/TMEM97 ligand with cytotoxic activity. *Eur. J. Pharmacol.* **2021**, *906*, No. 174263.

(5) Colom-Cadena, M.; Toombs, J.; Simzer, E.; et al. Transmembrane protein 97 is a potential synaptic amyloid beta receptor in human Alzheimer's disease. *Acta Neuropathol.* **2024**, *147*, No. 32.

(6) Izzo, N. J.; Xu, J.; Zeng, C.; et al. Alzheimer's Therapeutics Targeting Amyloid Beta 1−42 Oligomers II: Sigma-2/PGRMC1 Receptors Mediate Abeta 42 Oligomer Binding and Synaptotoxicity. *PLoS One* **2014**, *9*, No. e111899.

(7) Izzo, N. J.; Colom-Cadena, M.; Riad, A.; et al. Proceedings from the Fourth International Symposium on σ-2 Receptors: Role in Health and Disease. *eNeuro* **2020**, *7* (6), No. ENEURO.0317-20.2020, DOI: 10.1523/ENEURO.0317-20.2020.

(8) Alon, A.; Lyu, J.; Braz, J. M.; et al. Structures of the σ2 receptor enable docking for bioactive ligand discovery. *Nature* **2021**, *600*, 759−764.

(9) Cheng, Y.-S.; Zhang, T.; Ma, X.; et al. A proteome-wide map of 20(S)-hydroxycholesterol interactors in cell membranes. *Nat. Chem. Biol.* **2021**, *17*, 1271−1280.

(10) Riad, A.; Zeng, C.; Weng, C. C.; et al. Sigma-2 Receptor/TMEM97 and PGRMC-1 Increase the Rate of Internalization of LDL

by LDL Receptor through the Formation of a Ternary Complex. *Sci. Rep.* **2018**, *8*, No. 16845.

(11) Thejer, B. M.; Infantino, V.; Santarsiero, A.; et al. Sigma-2 Receptor Ligand Binding Modulates Association between TSPO and TMEM97. *Int. J. Mol. Sci.* **2023**, *24*, No. 6381.

(12) Li, J.; Shen, H.; Guo, L.-W. Transmembrane protein TMEM97 and epigenetic reader BAHCC1 constitute an axis that supports pro-inflammatory cytokine expression. *Cell. Signalling* **2024**, *116*, No. 111069.

(13) Mavlyutov, T. A.; Li, J.; Liu, X.; et al. Retinal Photoreceptor Protection in an AMD-Related Mouse Model by Selective Sigma-1 or Sigma-2 Receptor Modulation. *Genes* **2022**, *13*, No. 2386.

(14) https://cogrx.com/pipeline/dry-age-related-macular-degeneration.

(15) Pati, M. L.; Niso, M.; Spitzer, D.; et al. Multifunctional thiosemicarbazones and deconstructed analogues as a strategy to study the involvement of metal chelation, Sigma-2 (σ2) receptor and P-gp protein in the cytotoxic action: In vitro and in vivo activity in pancreatic tumors. *Eur. J. Med. Chem.* **2018**, *144*, 359−371.

(16) Pati, M. L.; Niso, M.; Ferorelli, S.; Abate, C.; Berardi, F. Novel metal chelators thiosemicarbazones with activity at the σ 2 receptors and P-glycoprotein: an innovative strategy for resistant tumor treatment. *RSC Adv.* **2015**, *5*, 103131−103146.

(17) Niso, M.; Kopecka, J.; Abatematteo, F. S.; et al. Multifunctional thiosemicarbazones targeting sigma receptors: in vitro and in vivo antitumor activities in pancreatic cancer models. *Cell. Oncol.* **2021**, *44*, 1307−1323.

(18) Ge, E. J.; Bush, A. I.; Casini, A.; et al. Connecting copper and cancer: from transition metal signalling to metalloplasia. *Nat. Rev. Cancer* **2022**, *22*, 102−113.

(19) Rodriguez, R.; Schreiber, S. L.; Conrad, M. Persister cancer cells: Iron addiction and vulnerability to ferroptosis. *Mol. Cell* **2022**, *82*, 728−740.

(20) Oliveri, V. Selective Targeting of Cancer Cells by Copper Ionophores: An Overview. *Front. Mol. Biosci.* **2022**, *9*, No. 841814, DOI: 10.3389/fmolb.2022.841814.

(21) Kopecka, J.; Barbanente, A.; Vitone, D.; et al. Cytotoxic pathways activated by multifunctional thiosemicarbazones targeting sigma-2 receptors in breast and lung carcinoma cells. *Pharmacol. Rep.* **2023**, *75*, 1588−1596.

(22) Anobile, D. P.; Niso, M.; Puerta, A.; et al. New Pharmacological Strategies against Pancreatic Adenocarcinoma: The Multifunctional Thiosemicarbazone FA4. *Molecules* **2022**, *27*, No. 1682.

(23) Roy, J.; Kyani, A.; Hanafi, M.; et al. Design and Synthesis of Orally Active Quinolyl Pyrazinamides as Sigma 2 Receptor Ligands for the Treatment of Pancreatic Cancer. *J. Med. Chem.* **2023**, *66*, 1990−2019.

(24) Hager, S.; Pape, V. F.; Pósa, V.; et al. High Copper Complex Stability and Slow Reduction Kinetics as Key Parameters for Improved Activity, Paraptosis Induction, and Impact on Drug-Resistant Cells of Anticancer Thiosemicarbazones. *Antioxid. Redox Signaling* **2020**, *33*, 395−414.

(25) Nunes, J. H. B.; Hager, S.; Mathuber, M.; et al. Cancer Cell Resistance Against the Clinically Investigated Thiosemicarbazone COTI-2 Is Based on Formation of Intracellular Copper Complex Glutathione Adducts and ABCC1-Mediated Efflux. *J. Med. Chem.* **2020**, *63*, 13719−13732.

(26) Alassadi, S.; Pisani, M. J.; Wheate, N. J. A chemical perspective on the clinical use of platinum-based anticancer drugs. *Dalton Trans.* **2022**, *51*, 10835−10846.

(27) Ghosh, S. Cisplatin: The first metal based anticancer drug. *Bioorg. Chem.* **2019**, *88*, No. 102925.

(28) Quiroga, A. G.; Ranninger, C. N. Contribution to the SAR field of metallated and coordination complexes. *Coord. Chem. Rev.* **2004**, *248*, 119−133.

(29) Pelosi, G. Thiosemicarbazone Metal Complexes: From Structure to Activity. *Open Crystallogr. J.* **2010**, *3*, 16−28.

(30) Salehi, R.; Abyar, S.; Ramazani, F.; et al. Enhanced anticancer potency with reduced nephrotoxicity of newly synthesized platin-based complexes compared with cisplatin. *Sci. Rep.* **2022**, *12*, No. 8316.

(31) Park, G. Y.; Wilson, J. J.; Song, Y.; Lippard, S. J. Phenanthriplatin, a monofunctional DNA-binding platinum anti-cancer drug candidate with unusual potency and cellular activity profile. *Proc. Natl. Acad. Sci. U.S.A.* **2012**, *109*, 11987−11992.

(32) Margiotta, N.; Natile, G.; Capitelli, F.; et al. Sterically hindered complexes of platinum(II) with planar heterocyclic nitrogen donors. A novel complex with 1-methyl-cytosine has a spectrum of activity different from cisplatin and is able of overcoming acquired cisplatin resistance. *J. Inorg. Biochem.* **2006**, *100*, 1849−1857.

(33) Margiotta, N.; Savino, S.; Gandin, V.; Marzano, C.; Natile, G. Monofunctional Platinum(II) Complexes with Potent Tumor Cell Growth Inhibitory Activity: The Effect of a Hydrogen-Bond Donor/ Acceptor N-Heterocyclic Ligand. *ChemMedChem* **2014**, *9*, 1161−1168.

(34) Hollis, L. S.; Sundquist, W.; Burstyn, J.; et al. Mechanistic Studies of a Novel Class of Trisubstituted Platinum(II) Antitumor Agents. *Cancer Res.* **1991**, *51*, 1866−1875.

(35) Poyraz, M.; Demirayak, S.; Banti, C. N.; et al. Platinum(II)-thiosemicarbazone drugs override the cell resistance due to glutathione; assessment of their activity against human adenocarci-noma cells. *J. Coord. Chem.* **2016**, *69*, 3560−3579.

(36) Bain, G. A.; West, D. X.; Krejci, J.; et al. Synthetic and spectroscopic investigations of N(4)-substituted isatin thiosemicarba-zones and their copper(II) complexes. *Polyhedron* **1997**, *16*, 855−862.

(37) Rodríguez-Argüelles, M. C.; Sánchez, A.; Ferrari, M. B.; et al. Transition-metal complexes of isatin-β-thiosemicarbazone. X-ray crystal structure of two nickel complexes. *J. Inorg. Biochem.* **1999**, *73*, 7−15.

(38) Singh, N. K.; Shrestha, S.; Shahi, N.et al. Study on Enhancement of Anticancer Activity of N(4)1-(2-Pyridyl)piperazinyl 5-Nitroisatin Thiosemicarbazone on Chelation with Copper(II). In *Challenges and Advances in Chemical Science*; Book Publisher International (a part of SCIENCEDOMAIN International, 2022; Vol. 9, pp 40−55.

(39) Pregosin, P. S. Platinum-195 nuclear magnetic resonance. *Coord. Chem. Rev.* **1982**, *44*, 247−291.

(40) Altomare, A.; Cuocci, C.; Giacovazzo, C.; et al. EXPO2013 : a kit of tools for phasing crystal structures from powder data. *J. Appl. Crystallogr.* **2013**, *46*, 1231−1235.

(41) Falcone, E.; Ritacca, A. G.; Hager, S.; et al. Copper-Catalyzed Glutathione Oxidation is Accelerated by the Anticancer Thiosemi-carbazone Dp44mT and Further Boosted at Lower pH. *J. Am. Chem. Soc.* **2022**, *144*, 14758−14768.

(42) Dharmasivam, M.; Kaya, B.; Wijesinghe, T. P.; et al. Differential transmetallation of complexes of the anti-cancer thiosemicarbazone, Dp4e4mT: effects on anti-proliferative efficacy, redox activity, oxy-myoglobin and oxy-hemoglobin oxidation. *Chem. Sci.* **2024**, *15*, 974−990.

(43) Gardner, B. M.; Pincus, D.; Gotthardt, K.; Gallagher, C. M.; Walter, P. Endoplasmic Reticulum Stress Sensing in the Unfolded Protein Response. *Cold Spring Harbor Perspect. Biol.* **2013**, *5*, No. a013169.

(44) Tesei, A.; Cortesi, M.; Zamagni, A.; et al. Sigma Receptors as Endoplasmic Reticulum Stress "Gatekeepers" and their Modulators as Emerging New Weapons in the Fight Against Cancer. *Front. Pharmacol.* **2018**, *9*, No. 711, DOI: 10.3389/fphar.2018.00711.

(45) Buondonno, I.; Gazzano, E.; Tavanti, E.; et al. Endoplasmic reticulum-targeting doxorubicin: a new tool effective against doxorubicin-resistant osteosarcoma. *Cell. Mol. Life Sci.* **2019**, *76*, 609−625.

(46) Li, M.; Tang, S.; Velkov, T.; Shen, J.; Dai, C. Copper exposure induces mitochondrial dysfunction and hepatotoxicity via the induction of oxidative stress and PERK/ATF4 -mediated endoplasmic reticulum stress. *Environ. Pollut.* **2024**, *352*, No. 124145.

(47) Ilamathi, H. S.; Germain, M. ER-mitochondria contact sites in mitochondrial DNA dynamics, maintenance, and distribution. *Int. J. Biochem. Cell Biol.* **2024**, *166*, No. 106492.

(48) Xu, S.; Hao, Y.; Xu, X.; et al. Antitumor Activity and Mechanistic Insights of a Mitochondria-Targeting Cu(I) Complex. *J. Med. Chem.* **2024**, *67*, 7911−7920.

(49) Jiang, X.-X.; Zhang, R.; Wang, H.-S. Neferine mitigates angiotensin II-induced atrial fibrillation and fibrosis via upregulation of Nrf2/HO-1 and inhibition of TGF-*β*/p-Smad2/3 pathways. *Aging* **2024**, *16*, 8630−8644.

(50) Shi, H.; Tang, H.; Ai, W.; et al. Schisandrin B Antagonizes Cardiotoxicity Induced by Pirarubicin by Inhibiting Mitochondrial Permeability Transition Pore (mPTP) Opening and Decreasing Cardiomyocyte Apoptosis. *Front. Pharmacol.* **2021**, *12*, No. 733805, DOI: 10.3389/fphar.2021.733805.

(51) Siegel, R. L.; Miller, K. D.; Fuchs, H. E.; Jemal, A. Cancer statistics, 2022. *Ca-Cancer J. Clin.* **2022**, *72*, 7−33.

(52) Siegel, R. L.; Giaquinto, A. N.; Jemal, A. Cancer statistics, 2024. *Ca-Cancer J. Clin.* **2024**, *74*, 12−49.

(53) Manrai, M.; Tilak, T.; Dawra, S.; Srivastava, S.; Singh, A. Current and emerging therapeutic strategies in pancreatic cancer: Challenges and opportunities. *World J. Gastroenterol.* **2021**, *27*, 6572−6589.

(54) Kukushkin, Y. N.; Vyaz'menskii, Y. E.; Zorina, L. I.; Pazukhina, Y. L. Complexes of palladium and platinum with dimethyl sulfoxide. *Russ. J. Inorg. Chem.* **1968**, *13*, 835−838.

(55) X-Ray Crystallographic Information Files FA4-Cu.Cif Contains the Supplementary Crystallographic Data for This Paper, and Are Supplied as Independent Supporting Information Files for This Article. These File Can Also Be Obtained Free of Charge from the Cam.

(56) Rietveld, H. M. A profile refinement method for nuclear and magnetic structures. *J. Appl. Crystallogr.* **1969**, *2*, 65−71.

(57) Altomare, A.; Campi, G.; Cuocci, C.; et al. Advances in powder diffraction pattern indexing: N-TREOR09. *J. Appl. Crystallogr.* **2009**, *42*, 768−775.

(58) Louer, D.; Boultif, A. Indexing with the successive dichotomy method, DICVOL04. *Z. Kristallogr. Suppl.* **2006**, *2006*, 225−230.

(59) *ACD/ChemSketch*; Advanced Chemistry Development, Inc.: Toronto, ON, Canada, 2003 www.acdlabs.com.

(60) Stewart, J. J. P.; MOPAC *Stewart Computational Chemistry*, Version 18.305L; Colorado Springs: CO, USA, 2016, Http://OpenMOPAC.Net/.

(61) Xu, X.; Tassone, B.; Ostano, P.; et al. HSD17B7 gene in self-renewal and oncogenicity of keratinocytes from Black versus White populations. *EMBO Mol. Med.* **2021**, *13*, No. e14133, DOI: 10.15252/emmm.202114133.

(62) Riganti, C.; Gazzano, E.; Gulino, G. R.; et al. Two repeated low doses of doxorubicin are more effective than a single high dose against tumors overexpressing P-glycoprotein. *Cancer Lett.* **2015**, *360*, 219−226.

(63) Riganti, C.; Costamagna, C.; Bosia, A.; Ghigo, D. The NADPH oxidase inhibitor apocynin (acetovanillone) induces oxidative stress. *Toxicol. Appl. Pharmacol.* **2006**, *212*, 179−187.

Supporting Information

First-in-class thiosemicarbazone metal complexes targeting the sigma-2 receptor (S2R) as an innovative strategy against pancreatic cancer

Alessandra Barbanente,[1,§] Joanna Kopecka,[2,§] Daniele Vitone,[1] Mauro Niso,[3] Rosanna Rizzi,[4] Corrado Cuocci,[4] Francesca Serena Abatematteo,[3] Francesco Mastropasqua,[3] Nicola Antonio Colabufo,[3] Nicola Margiotta,[1] Fabio Arnesano,[1] Chiara Riganti,[2*] Carmen Abate [3,4*]

[1] Department of Chemistry, University of Bari Aldo Moro, via E. Orabona, 4, 70125 Bari, Italy
[2] Department of Oncology, Molecular Biotechnology Center "Guido Tarone", piazza Nizza 44, 10126, Torino, Italy
[3] Department of Pharmacy-Pharmaceutical Sciences, University of Bari Aldo Moro, via E. Orabona, 4, 70125 Bari, Italy
[4] Institute of Crystallography-CNR, Via G. Amendola, 122/o, 70126 Bari, Italy

Corresponding authors Email: carmen.abate@uniba.it; chiara.riganti@unito.it
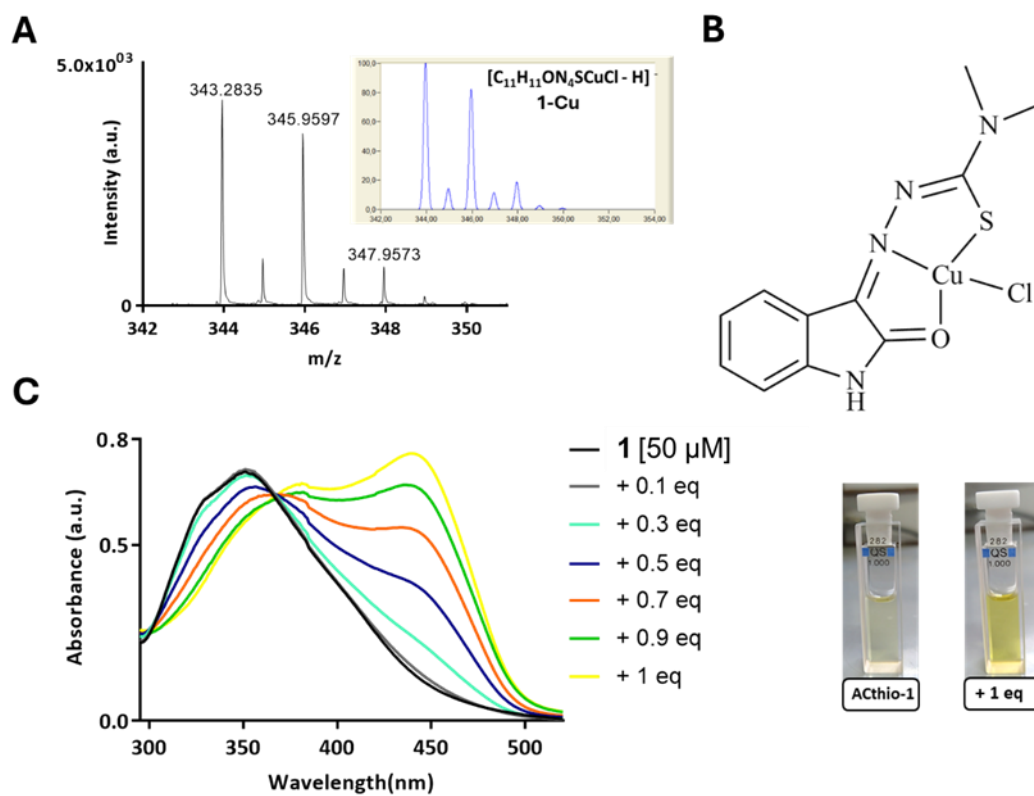
ASSOCIATED CONTENT

Figure S1. (A) ESI-MS spectrum of **1**-Cu in DMF. The inset shows the calculated isotope mass distribution for the specified molecular formula. (B) Proposed structure for **1**-Cu; (C) Overlay of UV-Vis spectra recorded on a solution of **1** in DMSO during titration with $CuCl_2$.
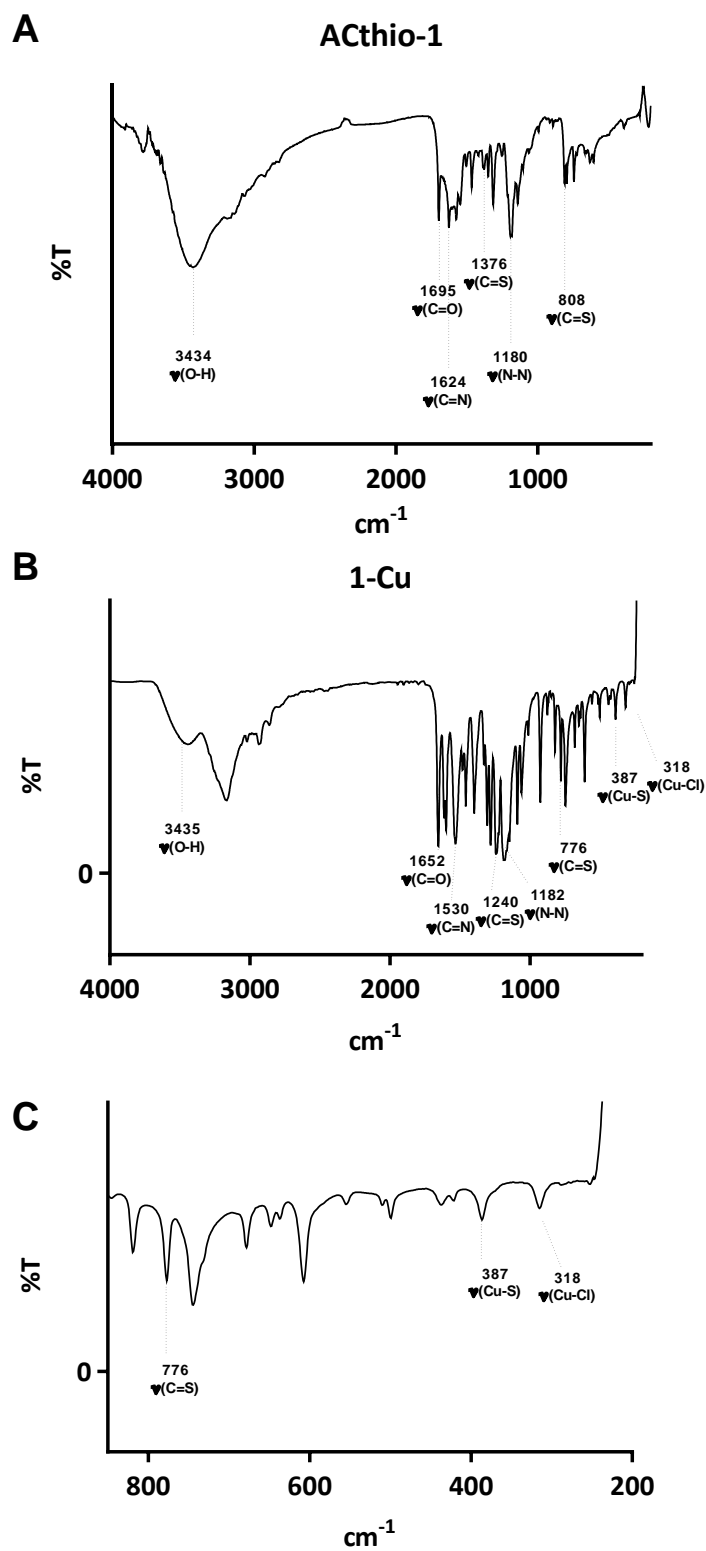
Figure S2. FTIR spectra of **1** (A), **1-**Cu (B), and magnified FTIR spectrum of **1-**Cu (C) in the range 850-200 cm⁻¹.
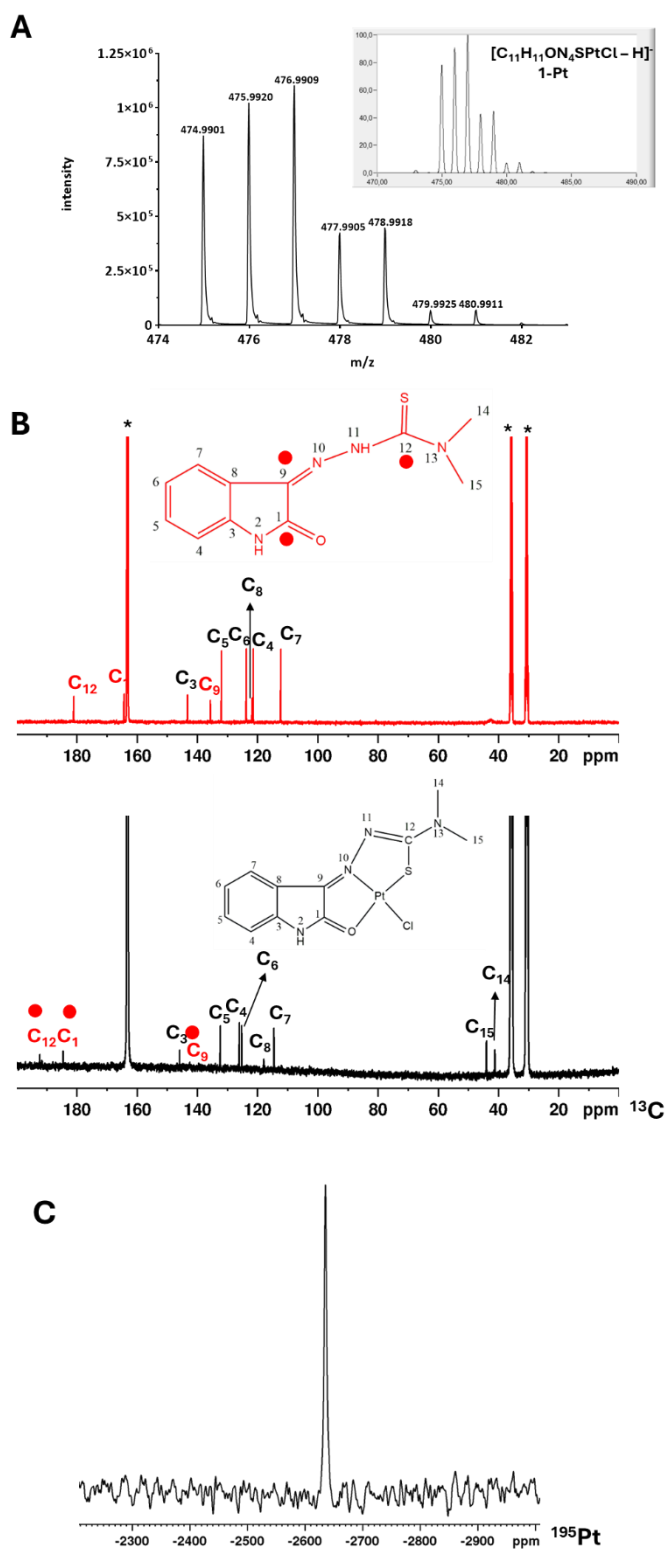
Figure S3. (A) ESI-MS spectrum of **1**-Pt in DMF. The inset shows the calculated isotope mass distribution for the specified molecular formula. (B) 1D ^{13}C NMR spectra of free **1** (red contours) and **1**-Pt (black contours) in DMF-d$_7$. The structural formulas with atom numbering are shown above each spectrum. ^{13}C signals that are more downfield shifted are marked with red dots. Assignments are indicated on top of each peak. (C) 1D ^{195}Pt NMR spectrum of **1**-Pt in DMF-d$_7$.
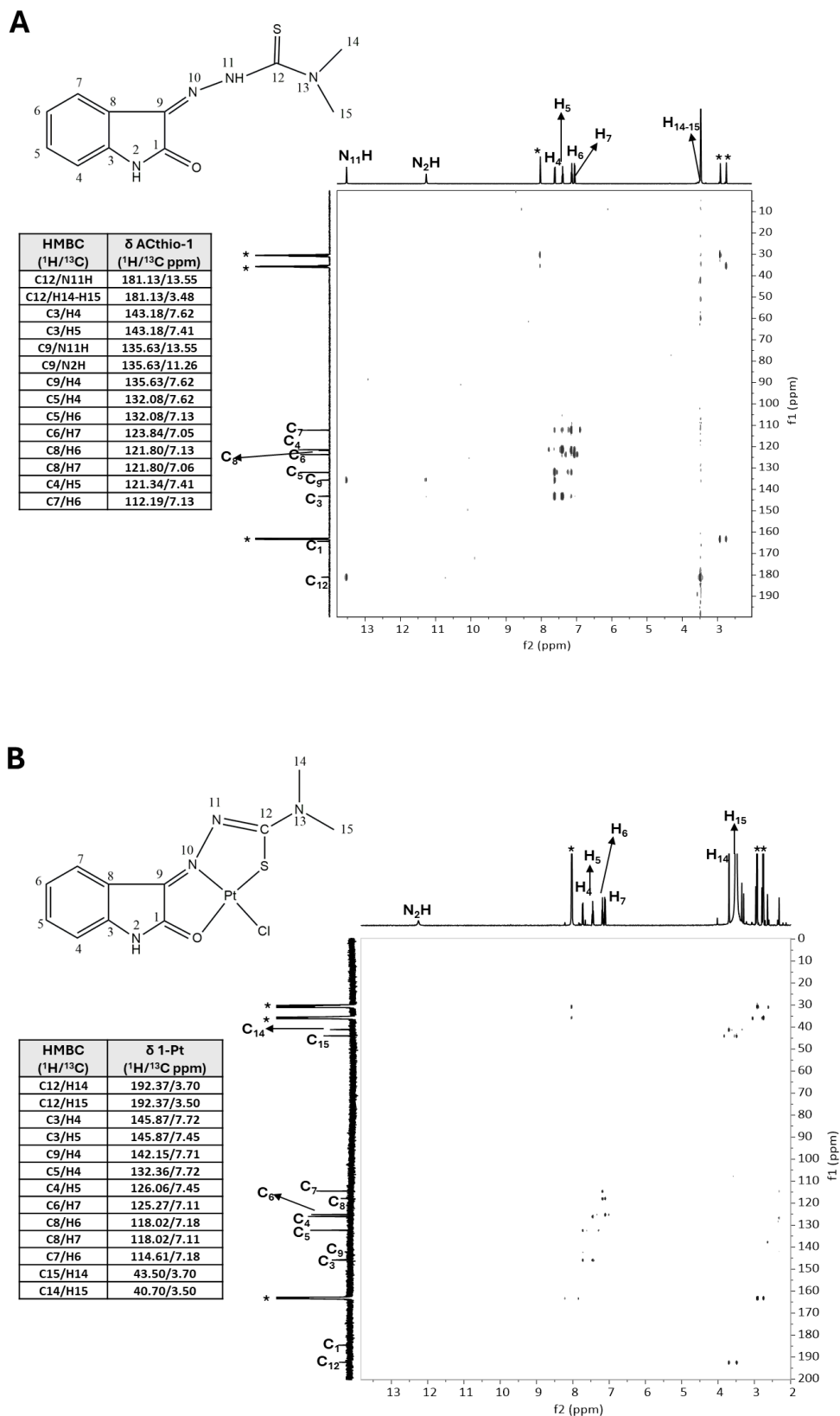
A

HMBC (^{1}H/^{13}C)	δ ACthio-1 (^{1}H/^{13}C ppm)
C12/N11H	181.13/13.55
C12/H14-H15	181.13/3.48
C3/H4	143.18/7.62
C3/H5	143.18/7.41
C9/N11H	135.63/13.55
C9/N2H	135.63/11.26
C9/H4	135.63/7.62
C5/H4	132.08/7.62
C5/H6	132.08/7.13
C6/H7	123.84/7.05
C8/H6	121.80/7.13
C8/H7	121.80/7.06
C4/H5	121.34/7.41
C7/H6	112.19/7.13

B

HMBC (^{1}H/^{13}C)	δ 1-Pt (^{1}H/^{13}C ppm)
C12/H14	192.37/3.70
C12/H15	192.37/3.50
C3/H4	145.87/7.72
C3/H5	145.87/7.45
C9/H4	142.15/7.71
C5/H4	132.36/7.72
C4/H5	126.06/7.45
C6/H7	125.27/7.11
C8/H6	118.02/7.18
C8/H7	118.02/7.11
C7/H6	114.61/7.18
C15/H14	43.50/3.70
C14/H15	40.70/3.50

Figure S4. 2D [^{1}H–^{13}C] HMBC NMR spectra of free compound **1** (A) and **1**-Pt (B) in DMF-d$_7$. The 1D ^{1}H and ^{13}C NMR spectra are shown at the top and left side of 2D spectra, respectively. Chemical shifts are listed in the tables according to the atom numbering shown in the structural formulas of the compounds.
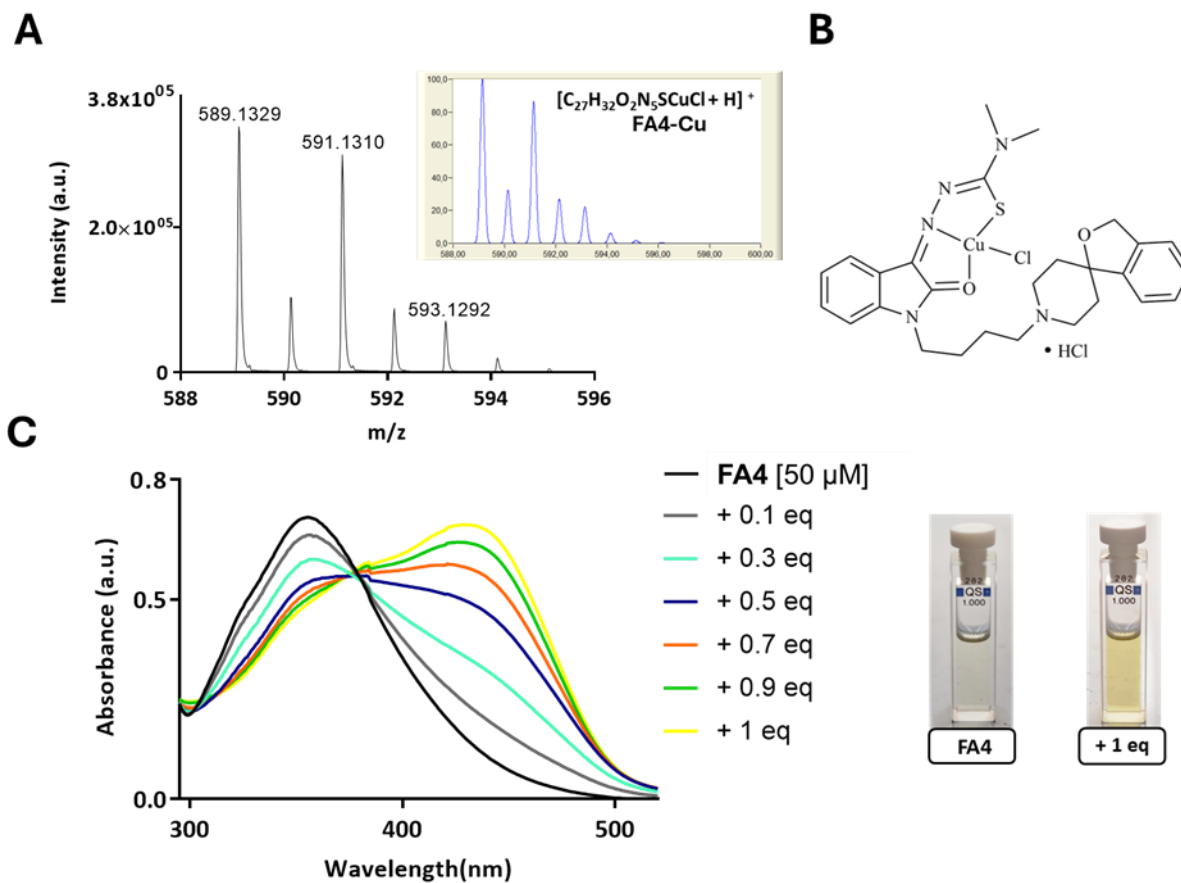
Figure S5. (A) ESI-MS spectrum of **FA4**-Cu in ethanol. The inset shows the calculated isotope mass distribution for the specified molecular formula. (B) Proposed structure for **FA4**-Cu; (C) Overlay of absorption spectra recorded on a solution of **FA4** in DMSO during titration with CuCl$_2$.
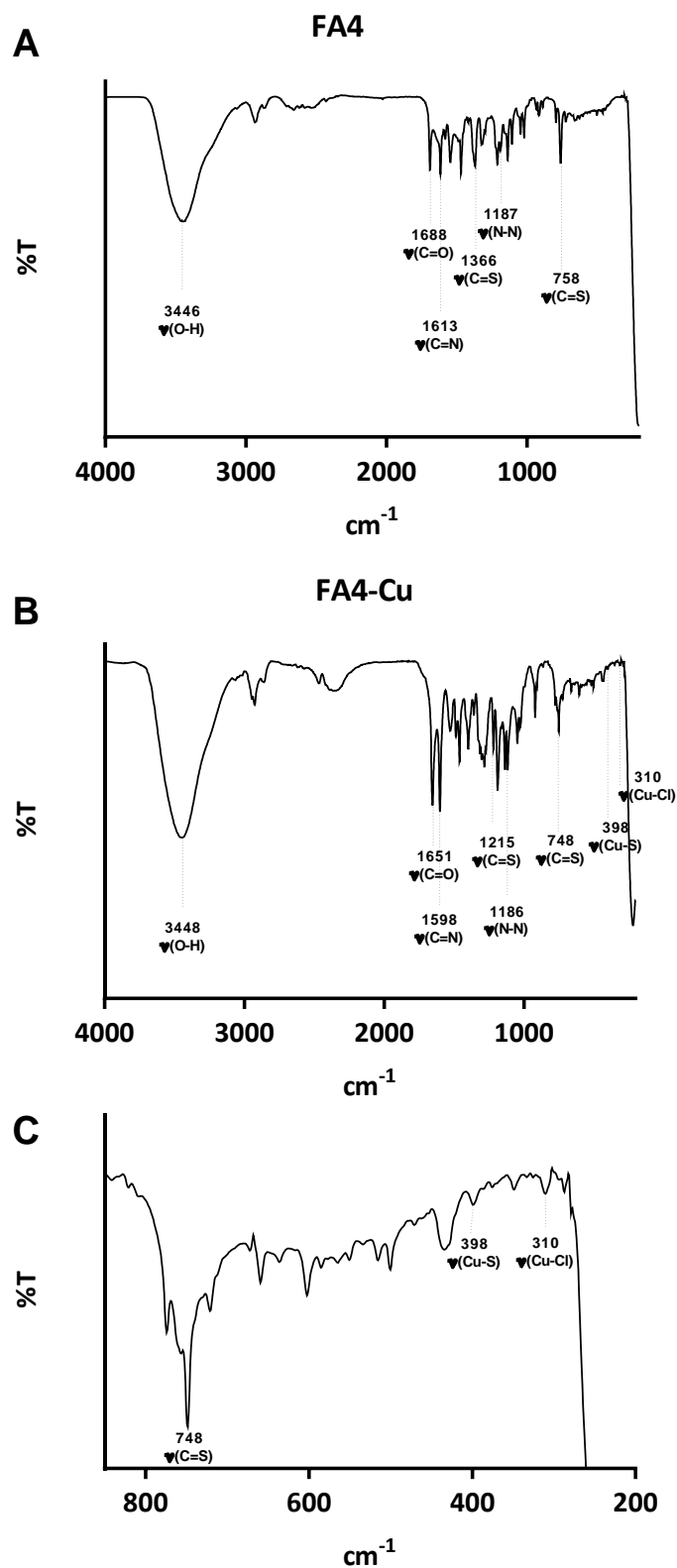
Figure S6. FTIR spectra of **FA4** (A), **FA4**-Cu (B), and magnified FTIR spectrum of **FA4**-Cu (C) in the range 850-200 cm^{-1}.
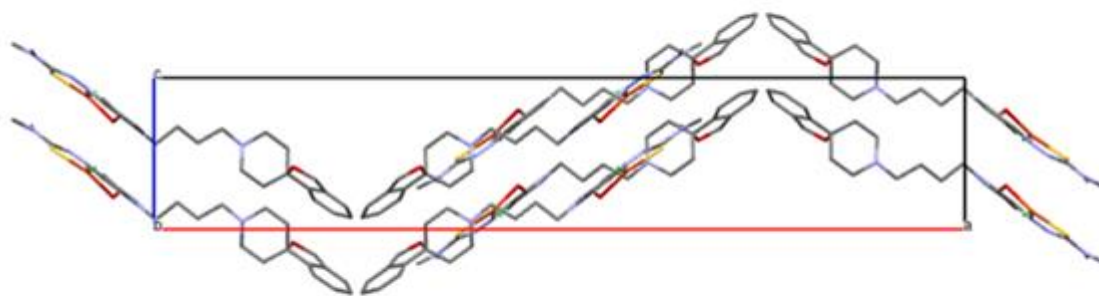
Figure S7. Crystal packing of **FA4**-Cu molecules viewed along the c axis, with hydrogen atoms omitted for clarity.
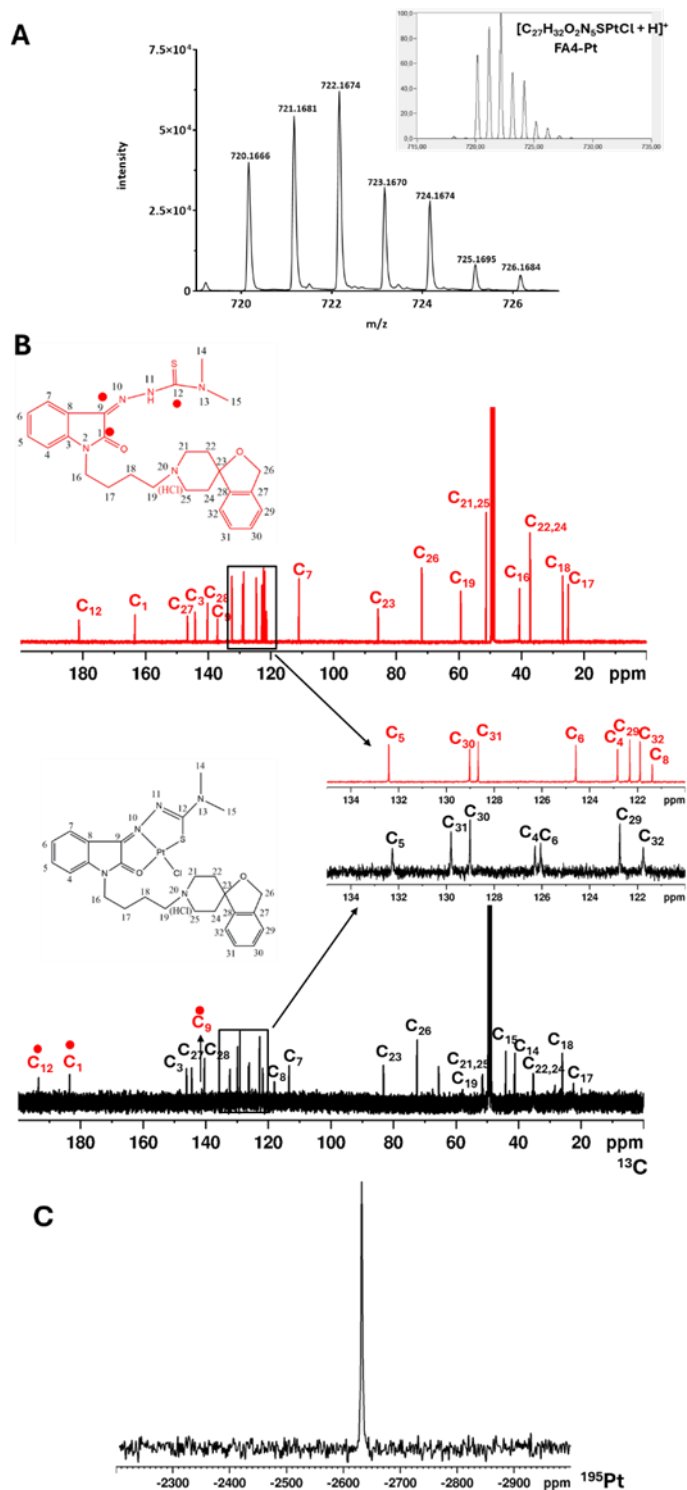
Figure S8. (A) ESI-MS spectrum of **FA4**-Pt in MeOH. The inset shows the calculated isotope mass distribution for the specified molecular formula. (B) 1D ^{13}C NMR spectra of free **FA4** (red) and **FA4**-Pt (black) in MeOH-d$_4$. The structural formulas with atom numbering are shown above each spectrum. ^{13}C signals more downfield shifted are marked with red dots. Assignments are indicated on the top of each peak. (C) 1D ^{195}Pt NMR spectrum of **FA4**-Pt in MeOH-d$_4$.
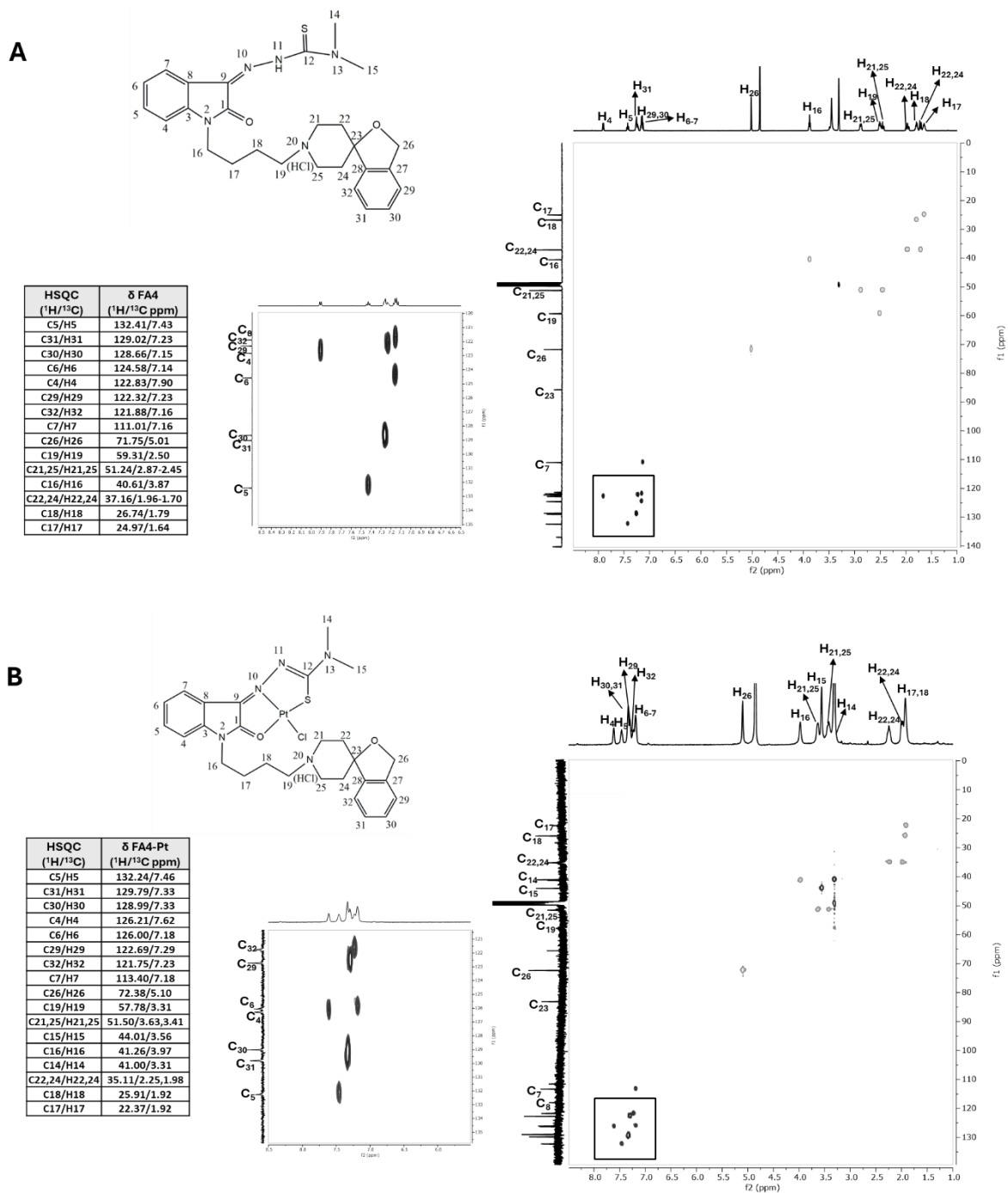
A

HSQC (^{1}H/^{13}C)	δ FA4 (^{1}H/^{13}C ppm)
C5/H5	132.41/7.43
C31/H31	129.02/7.23
C30/H30	128.66/7.15
C6/H6	124.58/7.14
C4/H4	122.83/7.90
C29/H29	122.32/7.23
C32/H32	121.88/7.16
C7/H7	111.01/7.16
C26/H26	71.75/5.01
C19/H19	59.31/2.50
C21,25/H21,25	51.24/2.87-2.45
C16/H16	40.61/3.87
C22,24/H22,24	37.16/1.96-1.70
C18/H18	26.74/1.79
C17/H17	24.97/1.64

B

HSQC (^{1}H/^{13}C)	δ FA4-Pt (^{1}H/^{13}C ppm)
C5/H5	132.24/7.46
C31/H31	129.79/7.33
C30/H30	128.99/7.33
C4/H4	126.21/7.62
C6/H6	126.00/7.18
C29/H29	122.69/7.29
C32/H32	121.75/7.23
C7/H7	113.40/7.18
C26/H26	72.38/5.10
C19/H19	57.78/3.31
C21,25/H21,25	51.50/3.63,3.41
C15/H15	44.01/3.56
C16/H16	41.26/3.97
C14/H14	41.00/3.31
C22,24/H22,24	35.11/2.25,1.98
C18/H18	25.91/1.92
C17/H17	22.37/1.92

Figure S9. 2D [^{1}H–^{13}C] HSQC NMR spectra of free **FA4** (A) and **FA4**-Pt (B) in MeOH-d$_4$. The 1D ^{1}H and ^{13}C NMR spectra are shown at the top and left side of 2D spectra, respectively. Chemical shifts are listed in the tables according to the atom numbering shown in the structural formulas of the compounds.

A

HMBC ($^1H/^{13}C$)	δ FA4 ($^1H/^{13}C$ ppm)
C12/H14,15	181.23/3.44
C1/H16	163.34/3.87
C27/H30	146.59/7.15
C27/H26	146.59/5.01
C3/H4	144.12/7.90
C3/H5	144.12/7.43
C3/H16	144.12/3.87
C28/H31	140.25/7.24
C28/H30	140.25/7.15
C28/H26	140.25/5.01
C9/H4	136.99/7.90
C5/H4	132.41/7.90
C31/H30	129.02/7.15
C31/H26	129.02/5.01
C30/H31	128.66/7.24
C30/H26	128.66/5.01
C6/H7	124.58/7.16
C4/H5	122.83/7.43
C29/H31	122.32/7.24
C29/H26	122.32/5.01
C32/H31	121.88/7.24
C32/H26	121.88/5.01
C8/H7	121.38/7.16
C7/H6	111.01/7.14
C23/H26	85.73/5.01
C23/H21,25	85.73/2.87
C23/H22,24	85.73/1.70
C19/H18	59.31/1.79
C19/H17	59.31/1.64
C21-25/H19	51.24/2.50
C21,25/H22,24	51.24/1.96
C16/H18	40.61/1.79
C16/H17	40.61/1.64
C22,24/H26	37.16/5.01
C18/H16	26.74/3.87
C18/H19	26.74/2.50
C17/H16	24.97/3.87
C17/H19	24.97/2.50
C17/H18	24.97/1.79
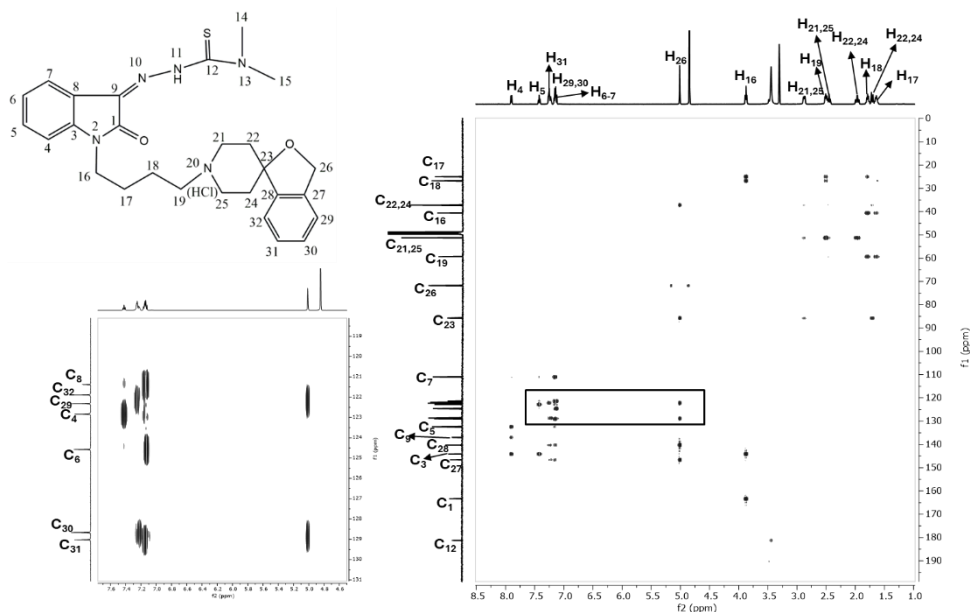
B

HMBC ($^1H/^{13}C$)	δ FA4-Pt ($^1H/^{13}C$ ppm)
C12/H15	193.40/3.56
C12/H14	193.40/3.31
C3/H4	146.09/7.62
C3/H5	146.09/7.46
C27/H30	144.40/7.33
C27/H26	144.40/5.10
C9/H4	141.14/7.62
C28/H30	140.38/7.33
C28/H26	140.38/5.10
C5/H4	132.24/7.62
C30/H26	129.79/5.10
C31/H29,32	128.99/7.29
C4/H5	126.21/7.46
C6/H7	126.00/7.18
C29/H30,31	122.69/7.33
C29/H26	122.69/5.10
C32/H31	121.75/7.33
C7/H6	113.31/7.18
C23/H26	83.12/5.10
C15/H14	44.01/3.31
C14/H15	44.01/3.56
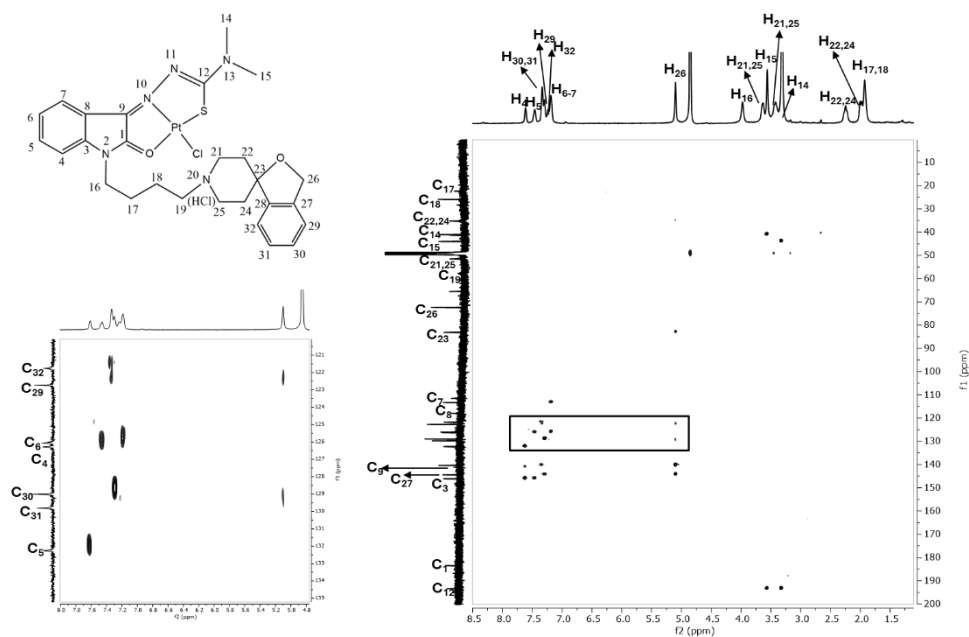
Figure S10. 2D [^1H–^{13}C] HMBC NMR spectra of free **FA4** (A) and **FA4**-Pt (B) in MeOH-d_4. The 1D ^1H and ^{13}C NMR spectra are shown at the top and left side of 2D spectra, respectively. Chemical shifts are listed in the tables according to the atom numbering shown in the structural formulas of the compounds.
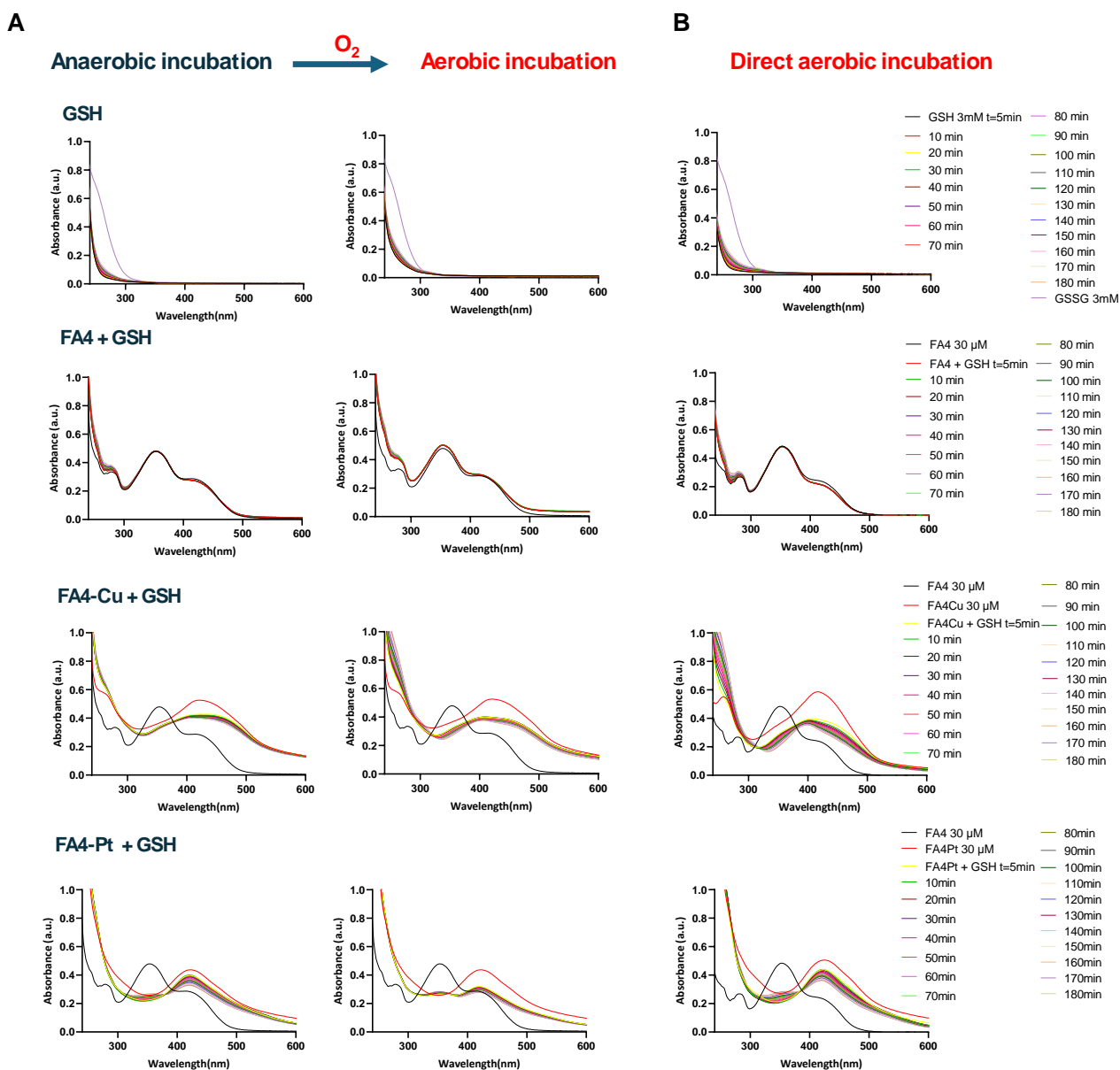
Figure S11. Time-dependent UV-Vis spectra for the indicated reaction mixtures incubated under anaerobic conditions followed by oxygen exposure (A), and under direct aerobic conditions (B). Buffer: 100 mM HEPES pH 7.4; DMSO/DMF 5%; [**FA4**/**FA4**-Cu/**FA4**-Pt] = 30 μM, [GSH] = 3 mM.
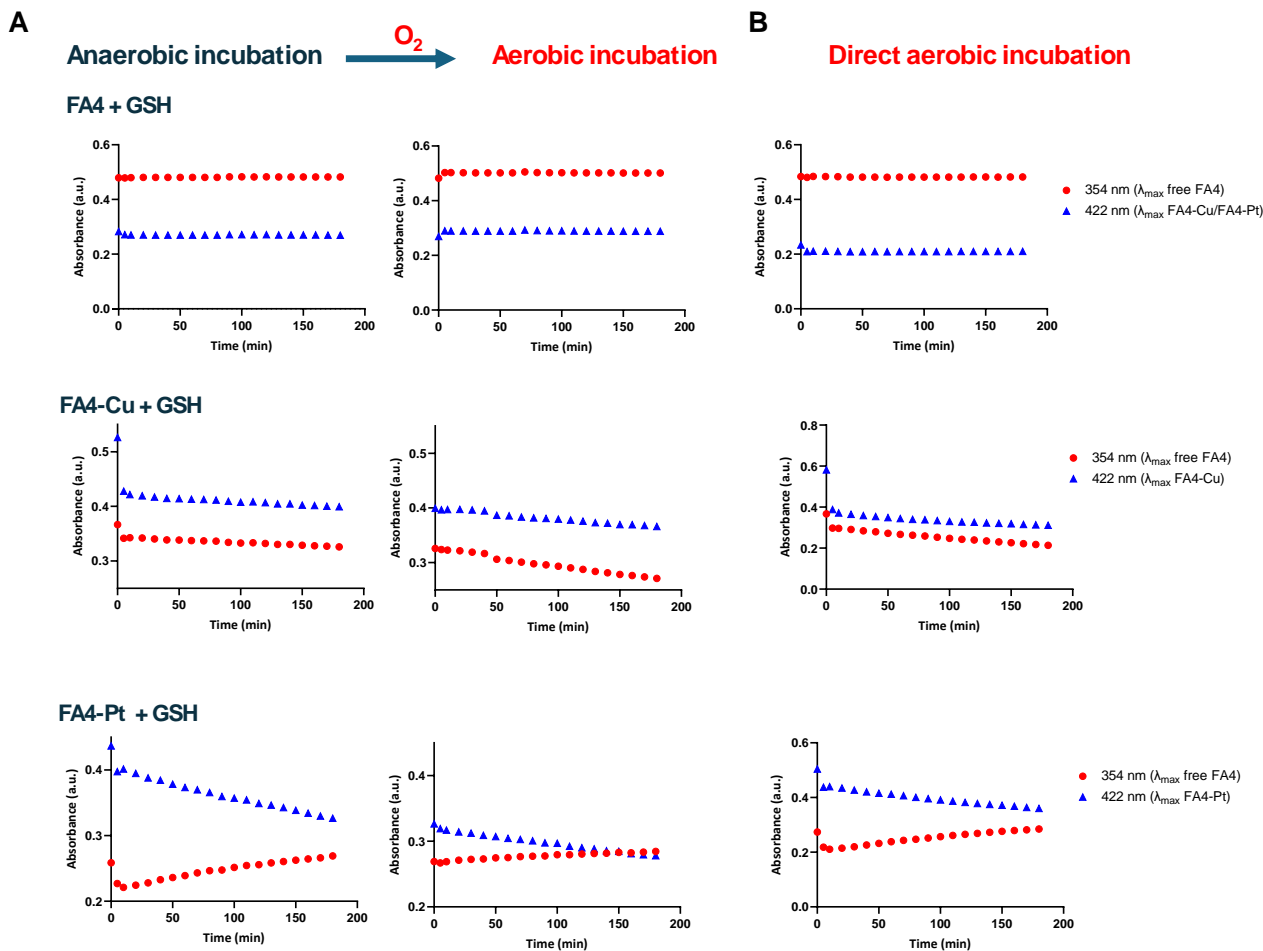
Figure S12. Time-dependent absorbance changes at 354 nm (λ_{max} of **FA4**) and 422 nm (λ_{max} of **FA4**-Cu and **FA4**-Pt), monitored by UV-Vis spectroscopy, for the indicated reaction mixtures incubated under anaerobic conditions followed by oxygen exposure (A), and under direct aerobic conditions (B). The increase in absorbance at 354 nm corresponds to the formation of free **FA4**. Buffer: 100 mM HEPES pH 7.4; DMSO/DMF 5%; [**FA4**/**FA4**-Cu/**FA4**-Pt] = 30 μM, [GSH] = 3 mM.
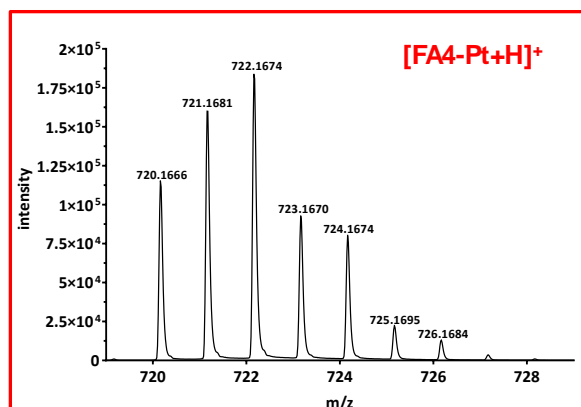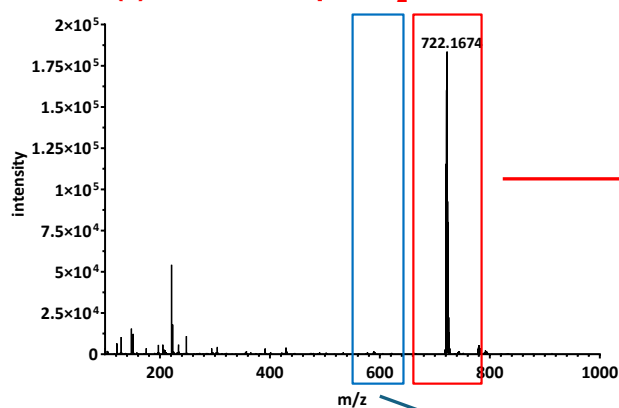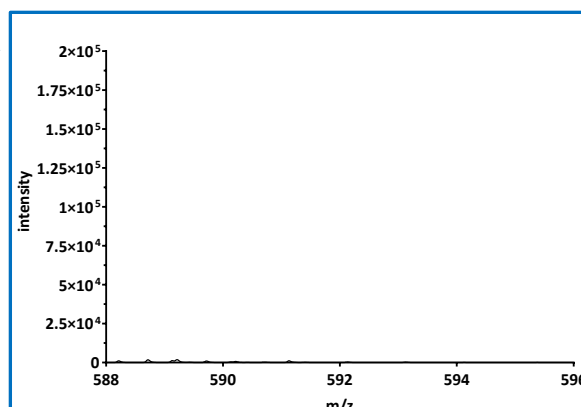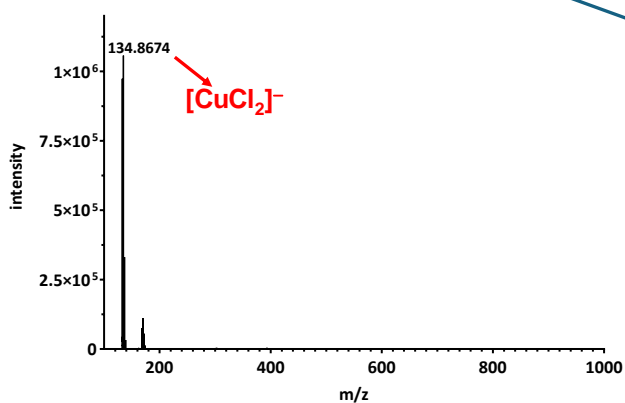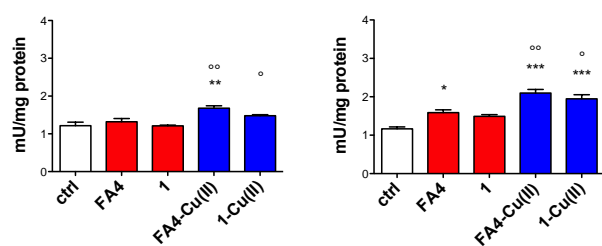
Figure S13. ESI-MS spectra of **FA4**-Pt incubated with CuCl₂ for 24 h, recorded in positive (+) and negative (−) ion modes in DMF/MeOH (50%/50%). The insets provide magnified views of the ESI-MS(+) spectrum in the m/z range of **FA4**-Pt (red box) and **FA4**-Cu (blue box), highlighting the isotope mass distribution of **FA4**-Pt and the absence of signals corresponding to **FA4**-Cu.

A

B

Mitochondrial SOD2

Cytosol SOD1
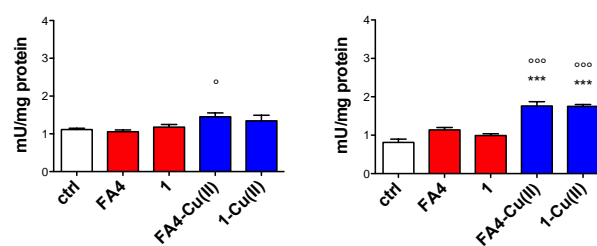
MiaPaCa-2

PANC-1

MiaPaCa-2

PANC-1

Figure S14. Effect of TSCs **FA4** and **1** and their Cu(II) complexes on the mitochondrial Cu-containing enzyme SOD2 (A) and the cytosolic Cu-containing enzyme SOD1 (B).
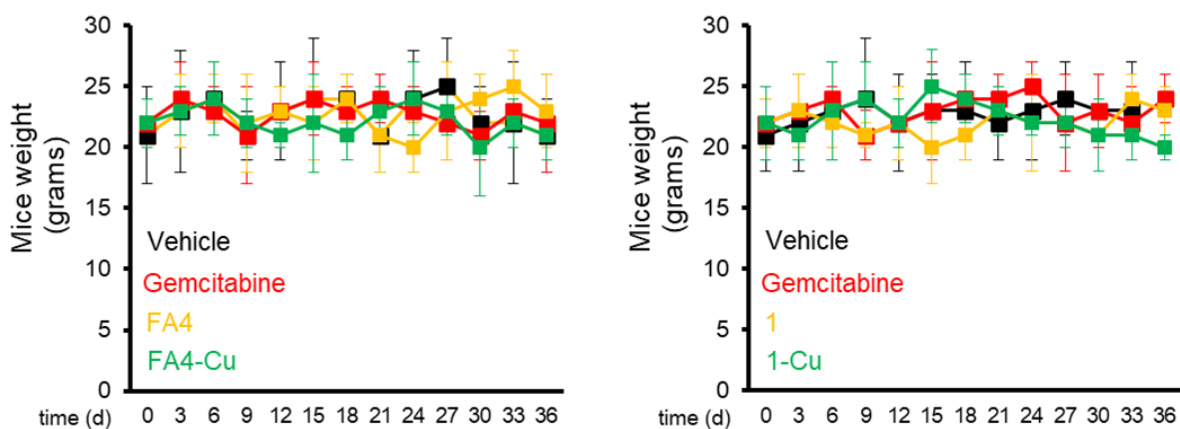
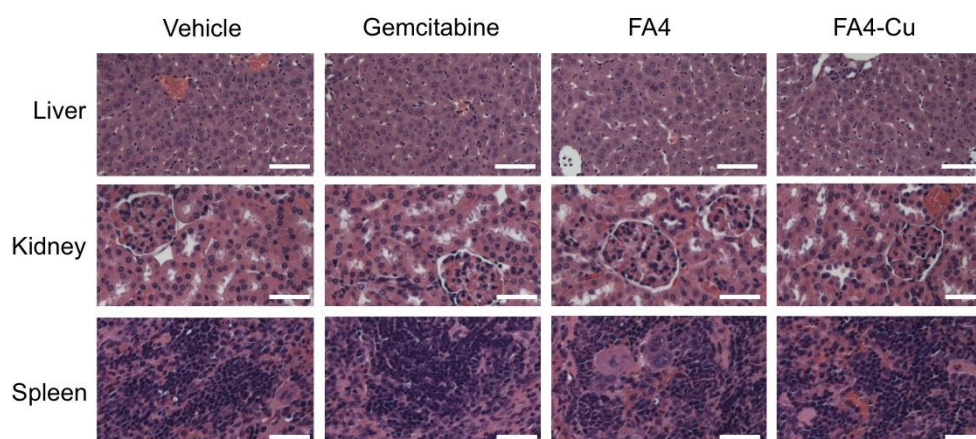**Figure S15**. Weight of the animals, treated as in Figure 10 (n= 5 animals/group of treatment).

Figure S16. Hematoxylin-eosin staining of the liver, kidney and spleen in animals treated as in Figure 10 (n= 5 animals/group of treatment). Bars: 100 μm (10x ocular, 20X objective fo spleen, 40X for liver and spleen).

Table S1. X-ray powder diffraction data parameters and refinement statistics for **FA4**-Cu

Crystal data	
CCDC number	2351856
Chemical formula	$C_{27}H_{32}ClCuN_5O_2S$
Formula weight (g/mol)	589.65
Crystal system	Orthorhombic
Space group	*Pbca*
Temperature (K)	293
Cell parameters (Å,°)	$a = 43.924\,(11)$ $b = 16.266\,(4)$ $c = 8.186\,(2)$
Volume (Å^3)	5849 (3)
Z	8
Z'	1
Radiation type	Cu $K\alpha_1$ radiation, $\lambda = 1.540560$ Å
Data collection	
Diffractometer	Rigaku RINT2500
Specimen mounting	special glass capillary
Data collection mode	transmission
2θ (°)	$2\theta_{min} = 6.00$, $2\theta_{max} = 80.00$
Structure solution	
Methods	Direct space method
Parameters	12+9 DOF
Cost function	$R_{wp} = 8.428$
Refinement	
R_p	3.866
R_{wp}	5.831
R_{exp}	2.907
χ^2	4.023
No. of data points	3701
No. of reflections	1780
Profile function	Pearson VII

Refinement parameters	
Lattice	3
Positional	111
ADP	6
Profile	10
Background	19
Peak-shift	3
Restraints	43
H-atom treatment	H-atom parameters constrained
Programs	
Indexing	N-TREOR09[48], DICVOL04[49]
Space group determination	EXPO[35]
Structure solution and refinement	EXPO
Model building	ChemSketch[50], MOPAC2016[51]
Structure visualization	Mercury[52]

Table S2. Hematochemical parameters of the animals measured immediately after euthanasia.

Paramater	Control	Gemcitabine	FA4	FA4-Cu
RBC (x10^6/µl)	3.98 ±1.73	4.45±0.51	3.98±0.83	4.11±1.14
Hb (g/dl)	12.39 ±3.78	11.98±3.45	11.94±3.22	13.15 ±3.04
WBC (x10^3/µl)	12.91 ±3.92	13.94 ±4.11	12.89 ±4.32	13.82 ±3.24
PLT (x 10^3/µl)	674±205	681±339	783±224	604±209
LDH (U/l)	5192±459	4983±403	6043±451	6281±547
AST (U/l)	201±36	182±44	182±43	154±29
ALT (U/l)	41±10	59±8	61±17	48±13
AP (U/l)	98±13	129±33	124±21	117±42
Creatinine (mg/l)	0.067±0.006	0.061±0.009	0.072±0.010	0.073±0.007
CPK (U/l)	342±67	314±56	324±32	312±48
c-TNT (ng/ml)	0.023±0.006	0.013±0.009	0.015±0.006	0.014±0.005